Direct pharmacological AMPK activation inhibits mucosal SARS-CoV-2 infection by reducing lipid metabolism, restoring autophagy flux and the type I IFN response

Andrea Cottignies-Calamarte[1,2], Flora Marteau[1,2], Sandrine Belouzard[3], Jean Dubuisson[3], Daniela Tudor[1,2], Benoit Viollet[2] and Morgane Bomsel[1,2,#]

[1]Laboratory of Mucosal Entry of HIV and Mucosal Immunity Institut Cochin, Paris France

[2]Université Paris Cité, CNRS, Inserm, Institut Cochin, Paris, France,

[3]Virologie moléculaire et cellulaire des coronavirus, Centre d'infection et d'immunité de Lille, Institut Pasteur de Lille, Université de Lille, CNRS, Inserm, CHRU, 59000 Lille, France

#: Corresponding author: morgane.bomsel@inserm.fr

Abstract

AMP-activated protein kinase (AMPK) plays a central role in regulating cell energy balance. When activated, AMPK supresses energy-consuming pathways such as lipid and protein synthesis while increasing nutrient availability through the activation of autophagy. These pathways downstream AMPK activation contribute to SARS-CoV-2 infection, which hijacks autophagy and accumulates lipid droplets in viral factories to support viral replication. Here, we assessed the antiviral activity of the direct pan-AMPK allosteric activator MK-8722 *in vitro.* MK-8722 efficiently inhibited infection of Alpha and Omicron SARS-CoV-2 variants in Vero76 and human bronchial epithelial Calu-3 cells at micromolar concentration. This inhibition relied on restoring the autophagic flux, which redirected newly synthesized viral proteins for degradation, and on a reduction in lipid metabolism, which affected the viral factories. Furthermore, MK-8722 treatment increased the type I interferon (IFN-I) response. Post-infection treatment with MK-8722 was enough to inhibit efficiently viral replication and restore the IFN-I response. Finally, MK-8722 treatment did not alter the SARS-CoV-2-specific $CD8^+$ T cell response mounted upon Spike vaccination. Overall, by activating AMPK, MK-8722 acts as an effective antiviral against SARS-CoV-2 infection, even when applied post-exposure, paving the way for preclinical tests aimed at inhibiting viral replication and improving patients' symptoms.

35 **INTRODUCTION**

36 The COVID-19 pandemic was efficiently contained due to the rapid development of vaccine and efficient
37 public health policies. However, despite these efforts, SARS-CoV-2 Variants Of Concern (VOC), which are
38 poorly sensitive to these vaccines, emerged and spread in the population, resulting in millions of deaths
39 [1]. Meanwhile, it has been challenging to develop an efficient antiviral treatment with an acceptable
40 benefit/risk ratio. As of January 2024, the treatment of patients in the intensive care unit (ICU) remains
41 primarily limited to drugs that either inhibit viral components such as Remdesivir and Paxlovid or target
42 SARS-CoV-2-induced cytokine storm, such as the IL-6 receptor antagonist Tocilizumab [1,2].

43 After its nasal entry, SARS-CoV-2 primarily infects lung epithelial cells in a mechanism by which the viral
44 envelope spike protein (Spike) binds to its main receptors angiotensin converting enzyme 2 (ACE2)
45 and/or transmembrane protease serine 2 (TMPRSS2). Following viral entry and the delivery of viral RNA
46 into the cytosol, the viral genes ORF1a and ORF1b are translated to the RNA-dependent RNA-
47 polymerase (RdRp). The viral RdRp further generates the remaining viral mRNA and the viral cycle
48 subsequently proceeds by hijacking cellular processes [2]. Replication of SARS-CoV-2, similar to other
49 enveloped RNA viruses, is supported by so-called viral factories with highly curved and three-
50 dimensional folded membrane extensions of modified endoplasmic reticulum [3,4], which formation
51 requires an increase in cell lipid metabolism. Viral factories compartmentalize viral genome from the
52 cytosol for replication and transcription, and provide protection against host cell defences. Disrupting
53 lipid metabolism hinders viral replication [5–7]. Accordingly, SARS-CoV-2 infection results in a significant
54 alteration in the cellular lipid repertoire in favor of polyunsaturated fatty acids, which are necessary for
55 the generation of infectious viruses [8–11]. This shift in lipid profile is mainly driven by the viral proteins
56 ORF9, nsp4 and nsp6, leading to the accumulation of lipid droplets in infected cells *in vitro* and in COVID-

57 19 autopsy tissues [5,12–15]. Accordingly, disrupting chemically either of these mechanisms inhibits SARS-
58 CoV-2 replication [5,11,12,14,16].

59 Throughout the SARS-CoV-2 viral cycle, autophagy is sequentially activated and inhibited. Indeed,
60 autophagy is initiated by the early expressed nsp6, resulting in the formation of autophagosomes that
61 are essential for the establishment of viral factories [17,18]. In turn, viral proteins OFR3a and ORF7a prevent
62 the fusion between autophagosomes and lysosomes thereby blocking completion of autophagy, as
63 evidenced by increased LC3-B expression, activation of the ULK1 kinase and increase in the autophagy
64 cargo receptor sequestosome-1/p62. Overall, this disruption of autophagy protects newly formed virus
65 from degradation in the LAMP1^{+} lysosome [19–23].

66 SARS-CoV-2 infection also impairs the expression of Interferon type 1 (IFN-I) and Interferon Stimulated
67 Genes (ISG), such as *Mx1* or *OAS1.* This reduction fails to restrict SARS-CoV-2 replication and this
68 contributes to the hyperinflammatory symptoms observed in COVID-19 [24–27]. Finally, SARS-CoV-2
69 infection interferes with the establishment of an efficient cellular response. By escaping lysosomal
70 degradation, SARS-CoV-2 limits viral peptide loading onto MHC-I and subsequent presentation to
71 specific cytotoxic CD8^{+} T Lymphocytes (CTL) [28,29]. In addition, SARS-CoV-2 ORF8 down-regulates MHC-I
72 expression from the plasma membrane, making infected cells less sensitive to SARS-CoV-2-specific CTLs
73 [30].

74 AMP-activated protein kinase (AMPK) is a highly conserved cellular energy sensor that plays a crucial
75 role in restoring the cellular energy balance by inhibiting ATP-consuming pathways (anabolism) and
76 activating ATP-producing pathways (catabolism) [31]. Notably, AMPK is a central regulator of lipid and
77 protein metabolism. AMPK inhibits fatty acid and cholesterol synthesis, by direct phosphorylation and
78 resulting inhibition of acetyl-CoA carboxylase (ACC) and 3-hydroxy-3-methylglutaryl-CoA (HMG-CoA)
79 reductase [31]. Additionally, AMPK is vital for the regulation of protein synthesis and cell growth through

80 the inactivation of mTORC1 signalling through phosphorylation of Tuberous Sclerosis Complex 2 (TSC2)
81 and Raptor [31]. Moreover, by activating Unc-51-like autophagy-activating kinase 1 (ULK1) and stimulating
82 Nuclear factor erythroid 2-related factor 2 (NRF2)-dependent p62 increased expression, AMPK
83 activation finely tunes cellular metabolic pathways [31]. AMPK appears as a critical hub of cellular
84 pathways affected by SARS-CoV-2 that are crucial for viral replication and pathogenesis.

85 A multitude of indirect and direct AMPK activators have been tested in preclinical models in various
86 domains including viral infection and metabolic diseases [31–33]. Recently, MK-8722, a direct allosteric-
87 activator of AMPK, has been developed [34]. MK-8722 is effective *in vitro* in the micromolar range on
88 AMPK activation, compared to the millimolar range for metformin and 5-aminoimidazole-4-carboxamide
89 riboside (AICAR) [34,35]. MK-8722 has already been orally tested at 10 mg/kg in preclinical models of
90 diabetes, resulting in improvements of glycemia but with a minor and reversible cardiac hypertrophy [34].

91 Here, we investigated whether allosteric AMPK activation by MK-8722 inhibits SARS-CoV-2
92 infection/replication by promoting autophagy of viral particles and restoring normal lipid metabolism
93 and the IFN-I response.

94

95 **MATERIAL AND METHODS**

96 **Cell culture and chemical compounds**

97 All cells were cultured at 37°C in a humid atmosphere with 5% CO2. Vero76 (ATCC CRL-1587), Calu-3
98 (ATCC HTB-55) and Caco2 (ATCC HTB-37) cells were cultured in DMEM (Gibco 41966-029) containing 1%
99 Penicillin-Streptomycin (PS) (Gibco 15140122) and decomplemented Foetal Calf Serum (FCS) (Eurobio
100 CVFSVF06-01) at 10% (D10) for Calu-3 and Vero76 cells, and at 20% (D20) for Caco2 cells. Caco2 cells

101 culture medium was supplemented with 1% MEM Non-Essential Amino Acids (Gibco 11140035). All viral
102 inoculations and infections were made in DMEM containing 2% FCS (D2).

103 Peripheral blood mononucleated cells (PBMCs) of healthy donor were collected from the French blood
104 bank (Etablissement Français du Sang, EFS) after initiation of SARS-CoV-2 vaccination in the global
105 population (June 2021). PBMCs were obtained by Ficoll gradient centrifugation, aliquoted and stored in
106 StemMACS CryoBrew (Miltenyi, 130-109-558) until use. $CD8^+$ T cells were isolated from HLA-$A2^+$
107 individuals using CD8 microbeads (Miltenyi 130-045-201) following manufacturer instructions. Cells
108 ($5x10^6$ cells at 10^6 cells/mL) were further expanded with TransAct (Miltenyi, 130-111-160, 1:100 dilution)
109 for 15 days in RPMI 10% FCS, 2 mM L-Glutamine (R10) (Thermo 25030081) + 10 IU/mL IL-2 (Roche
110 11011456001) after CD3/CD28 stimulation. TransAct was then washed out and cells frozen (1 million
111 cells/vial) as decribed above. CD14-depleted PBMCs from healthy donors were obtained by collecting
112 the flow-through of CD14 magnetic isolation (Miltenyi, 130-050-201). Resulting cells were then frozen as
113 decribed above.

114 The absence of Mycoplasma in the cell lines was routinely controlled using the MycoAlert mycoplasma
115 detection kit (Lonza, LT07-318).

116 Remdesevir and MK-8722 were purchased at MedChemExpress (respectively HY-104077 and HY-
117 111363) and solubilized in DMSO at 10 µg/mL.

118

119 **Virus Propagation**

120 SARS-CoV-2 variant Alpha and Omicron were obtained as we described [36,37], viral stocks prepared by
121 amplification on Vero76 cells as we described [35,], aliquoted and cryopreserved at -80°C. Viral stocks were
122 titrated on Vero76 cells after thawing as we described [35].

123

124 **Foci Forming Assay**

125 Hundred thousand of Vero76 cells were seeded in 48 well-plates one day before infection, resulting in
126 confluent cells at the day of infection. Virus-containing supernatant from infected cells to be tested
127 were diluted at least 1,000 times in 100 µl of D2 and added to cells for 2h and then replaced with an
128 overlay medium (300 µl) composed of 0.3% Low Melting Agarose (Sigma A0701) in D2 at 37°C. Plates
129 were then placed at 4°C for 10 min to allow overlay medium to solidify and further incubated for 18h at
130 37°C. Plates were washed 3 times with PBS (Gibco 25300) to remove overlay, fixed with 4%
131 paraformaldehyde (PFA) (Electron Microscopy Sciences 15710) in PBS (PBS-4% PFA) for 1h at room
132 temperature and permeabilized with 0.1 % Triton-X100 in PBS for 10 min. Cells were washed 3 times
133 and the viral nucleocapsid was labelled using an biotinylated-anti-N-antibody at 300 ng/mL (Bioss bsm-
134 41411M-biotin) in PBS supplemented with 0.1% Saponin (Sigma S-7900), 2% FCS, and 2 mM EDTA (Perm
135 Buffer) for 30 min at room temperature. Cells were washed three times in PBS, incubated with
136 streptavidin-coupled-HRP 0.1 µg/mL (Vector Laboratories, INC, Burlingame, CA, 94010) in Perm Buffer
137 for 30 min, washed again, and incubated with 100 µl/well of KPL TMB TrueBlue (Sera Care 5510-0030)
138 for 30 min at 37°C.

139 The infectious index was established as the ratio of the viral copy number/mL over the FFU/mL titre
140 computed from paired datasets obtained in RT-qPCR and titration experiments.

141

142 **Inhibition assay**

143 Vero76 and Calu-3 cells were plated respectively at least 1 and 5 days before infection. Cells were
144 treated with MK-8722 either continuously or only after infection (post-infection). Continuous treatment

145 consisted in treatment at indicated concentrations for 1h before infection at 37°C, during the 2h
146 inoculation, and until endpoint. Fully confluent cell layers were infected with an MOI of 0.001 for Vero76
147 cells or of 0.05 for Calu-3 in D2 for 2h. Inoculates were replaced by fresh D2 containing or not MK-8722,
148 and cells further incubated for 1 and 4 days for Vero76 and Calu-3 cells, respectively. Before harvesting
149 cells, supernatants were collected, clarified by centrifugation, and stored at -80°C for further RT-qPCR
150 quantification and viral titration.

151 When indicated, untreated or pre-treated cells with 1 µM or 5 µM MK-8722 (for Vero76 and Calu-3 cells,
152 respectively) were inoculated at 4°C for 1h to allow virus attachment to the cell membrane, wash three
153 times in ice cold PBS and fresh D2, with or without MK-8722, was added before rising the temperature
154 to 37°C for 1h or 24h for Vero76 and for 32h for Calu-3 cells, as indicated. Cells were then harvested and
155 processed for *N* RNA quantification as described below. For post-infection treatments, MK-8722 was
156 added at 8h post-infection (hpi) or 1 day post-infection (dpi), to reach indicated concentrations, controls
157 receiving the same volume of D2.

158

159 **Quantification of infection by flow cytometry**

160 Single-cell staining for viral protein and RNA by FISH-Flow was performed as described [36].

161 Briefly, cells were detached with trypsin 0.05% (Gibco 25300-024) for 10 min at 37°C and placed in 96
162 wells-plates. After centrifugation, cells were stained for 5min on ice for viability (Viobility 405/452,
163 Miltenyi 130-130-420, diluted 100 times in cold PBS). Cells were washed in PBS and fixed with PBS-4%
164 PFA. Cells were washed in Perm Buffer and labelled for 30min with anti-spike-AF488 antibody (R&D
165 FAB105403G) diluted 250-fold in Perm Buffer and washed in Perm Buffer.

166 To further label viral RNA, cells were washed twice in Hybridization Wash Buffer (HWB) (2X SSC, 10%
167 formamide (MP Biomedicals FORMD002), 0.2 mg/mL Bovine Seric Albumin (BSA) UltraPure
168 (ThermoFisher Scientific AM2618) in ultrapure water (Invitrogen 10977-035)), resuspended in
169 hybridization buffer (10% (w/v) Dextran sulfate (Calbiochem 265152), 1 mg Yeast tRNA (Invitrogen
170 AM2616), 2X SSC, 10% Formamide, 0.2 mg/mL BSA RNase-free in ultrapure water) with 50 nM total
171 SARS-CoV-2-quasar670-specific FISH probes (Stellaris) in equimolar proportion, targeting regions of S,
172 ORF1 and N genes, resuspended in hybridization buffer and incubated for 12-16h at 37°C. After three
173 wahses in HWB, cells were resuspended in PBS and analysed by flow cytometry. Proportion of infected
174 cells was quantified by flow cytometry (Guava 12-HT flow cytometer, Millipore) and analysed using the
175 native GuavaSoft 3.4 software.

176

177 **Western-blotting**

178 Cells were washed 3 times in PBS and lyzed with 1% Triton X-100 in 50 mM Tris pH 7.4, 150 mM NaCl, 1
179 mM EDTA, 1 mM EGTA, 10% Glycerol, 1 mM DTT, 1% Proteases Inhibitor Cocktail (Sigma P8340), 1%
180 Phosphatases inhibitor cocktail II and III (Sigma P5725 et P0044 respectively). Cell lysates were clarified
181 by centrifugation at 15,000g for 10min at 4°C, aliquoted and stored at -80°C. Protein content was
182 quantified by BCA assay after sample thawing (Thermo Fischer J61522.AP). Around 25µg protein were
183 separated by SDS-PAGE 12% at 100 mV and transferred on nitrocellulose membranes in wet condition at
184 80 mA at 4°C for 3h. Membranes were then saturated with TBS-0.5% Tween-20 (Sigma P1379, TBS-T)-5%
185 BSA. After three washes in TBS-T, membranes were incubated with primary antibodies described in
186 table 1 for 16h at 4°C. After three washes in TBS-T, relevant secondary antibody conjugated to HRP (see
187 **Table 1**) was added for 1h at room temperature followed by washed 3 times in TBS-T. Finally,
188 membranes were incubated with the West PicoPlus ECL HRP substrate (Thermo Fischer 34580). Signal

189 was imaged with Fusion FX (Villber Lourmat) and quantified using Fiji ImageJ software. When indicated,
190 data were computed from the Log2 fold change of the condition of interest over Non-infected non-
191 treated cells and presented as heat map using GraphPad8.

192

Table 1: Antibody list used for western-blotting

Target	Host and antibody nature	Conjugation	Supplier & reference	Dilution
β-actin	Goat polyclonal	-	Abcam ab8229	4,000
p-Thr172-AMPK	Rabbit polyclonal	-	CST 2531	5,000
Pan-AMPK	Rabbit polyclonal	-	CST 2532	5,000
p-Ser79-ACC	Rabbit polyclonal	-	CST 11818	5,000
Pan-ACC	Rabbit polyclonal	-	CST 3676S	5,000
p-Ser555-ULK1	Rabbit polyclonal	-	CST 5869	5,000
Pan-ULK1	Rabbit polyclonal	-	CST 4773	5,000
p-Ser792-Raptor	Rabbit polyclonal	-	CST 2083	5,000
Nucleocapsid	Mouse IgG2b	Biotin	BIOSS bsm-41411M-biotin	3,000 (300 ng/mL)
Pan-Raptor	Rabbit polyclonal	-	CST 2280	5,000
SQSTM1/p62	Rabbit polyclonal	-	CST 5114	5,000
Goat	Monkey polyclonal	HRP	Promega V805A	5,000
Rabbit	Donkey polyclonal	HRP	Southern Biotech 6440-05	5,000
Streptavidin	-	HRP	Vector Laboratories, INC, Burlingame, CA, 94010	10,000

193

194 **RNA extraction, N normalizer plasmid and RT-qPCR**

195 For RNA extraction, cells were washed 3 times in PBS and lysed in RA1 buffer. RNA was then extracted
196 using Nucleospin RNA kit (Macherey-Nagel 740955) following manufacturer instructions, and stored at -
197 80°C before RT-qPCR experiments. Primers and probes, designed according to original CDC

198 recommendations[38], are described in **Table 2** (Eurofins Genomics). Normalizer plasmid was obtained
199 after T-A cloning of the corresponding cDNA using High Capacity RNA-to-cDNA kit (Thermo Fischer
200 387406) amplified using regular N-directed PCR with Platinium Taq (Thermo Fischer 10966034) following
201 the TOPO cloning kit instruction (Thermo Fischer 10966034) and transformation of homemade
202 thermocompetent TOP10 bacteria. Clones were selected using white-blue screening on LB agar plates
203 with 100 µg/mL ampicillin and 20 µg/mL X-Gal (Thermo Fisher R0941). Plasmids were extracted using
204 NucleoSpin Mini kit (Macherey Nagel 740588) and controlled by Sanger sequencing (Eurofins Genomics).
205 For *Nucleocapsid* RNA relative or absolute quantification, RT-qPCR was performed using 4µl of cellular
206 RNA and Taqman RNA-to-Ct 1step kit (Thermo Fischer 4392938) following manufacturer
207 recommendations using a LightCycler 480 (Roche). For IFN-I and ISG expression analysis, reverse
208 transcription was first carried out using High-Capacity RNA-to-cDNA and further quantified using Sybr
209 Master mix I (Roche #04707516001). Relative gene expression over *β-actin* in cell lysates was calculated
210 by the $2^{-\Delta\Delta Ct}$ method while absolute *N* abundance in supernatants was quantified using the N normalizer
211 plasmid.

Table 2: Primer characteristics

Target	Name	Sequence	Tm (°C)
Nucleocapsid	N2-Fow	TTACAAACATTGGCCGCAAA	53.2
	N2-Rev	GCGCGACATTCCGAAGAA	56
	N2-Probe	ACAATTTGCCCCCAGCGCTTCAG	64.2
β-Actin	βAct-Fow	TGTTTGAGACCTTCAACACC	55.3
	βAct-Rev	ATGTCACGCACGATTTCC	53.7
	βAct-Probe	CCTCACCGAGCGCGGCTACAGCTTCA	72.9
IFN-α	IFN-α Fow	ACAACCTCCCAGGCACAAGGGCTGTATTT	72.5
	IFN-α Rev	TGATGGCAACCAGTTCCAGAAGGCTCAAG	71.2
IFN-β	IFN-β Fow	GTTCCTTAGGATTTCCACTCTGACTATGGTCC	68.6
	IFN-β Rev	GAACTTTGACATCCCTGAGGAGATTAAGCAGC	68.6
Mx1	Mx1 Fow	CTGGTGCTGAAACTGAAGAAAC	60.8
	Mx1 Rev	TACCTCTGAAGCATCCGAAATC	60.9
OAS1	OAS1 Fow	TCCACCTGCTTCACAGAACTACA	64.5
	OAS1 Rev	GGCGGATGAGGCTCTTGAG	63

212

213 **Immunofluorescence**

214 Calu-3 cells were plated on Poly-L-Lysine (Sigma P8920) (0.1% in H_20) coated Ibidi slides (Ibidi 80841) at
215 $1.2x10^5$/well for 5 days and infected with SARS-CoV-2 as described above. At 3dpi, cells were washed,
216 stained with 10 µg/mL Nile Red (Sigma 72485) in PBS at 37°C for 20 min, and washed prior fixation,
217 when indicated. Cells were fixed in PBS-4% PFA for 1h, washed and permeabilized using 0.1% TritonX-
218 100 in PBS for 10 min. Non-specific binding was blocked with 5% FCS in PBS for 30 min. Cells were
219 further labelled in Perm Buffer with biotinylated-anti-N antibody at 300 ng/ml (BIOSS bsm-41411M-
220 biotin) and/or anti-LAMP1 at 625 ng/mL (BD 555798), overnight at 4°C and the relevant secondary for
221 1h at room temperature (Streptavidin-AF488 Invitrogen S11223 at 2 µg/mL final, anti-mouse IgG1-Cy5
222 Abcam ab136127 at 1.5 µg/mL final). After nuclear staining with DAPI, cells were washed, and slides
223 mounted with Ibidi mounting medium (Ibidi 50001). Staining was observed by confocal microscopy
224 (Xplore confocal microscope). At least five randomly chosen fields per condition were imaged and
225 further analysed using ImageJ software and the particle analysis function. Lipid droplets (LD) were
226 identified as Nile Red positive vesicular objects with diameter > 500 nm. Lysosomes were identified as
227 LAMP1 positive vesicular objects with diameter > 700 nm. Analyse of lysosomes and LD was performed
228 using Z-projections made from 6 consecutive slices 300 nm apart. The number of particles per infected
229 cells, their mean area and intensity were then calculated. Colocalization on z-stack images was analysed
230 with the JACoP plugin using object-based colocalization and setting threshold at 137, 134 and 120 for
231 Lysosomes, LD and nucleocapsid objects, respectively. Manders' Overlap Coefficients (MOC)
232 corresponding respectively to green objects colocalizing in red objects and inversely red objects
233 colocalizing in green objects were computed.

234

235 **Lysosomal function analysis**

236 Confluent Calu-3 cells in a 96-well plate were inoculated with either Alpha or Omicron variant at 0.05
237 MOI for 2h, and cells were further cultured with fresh D2 up to 24hpi. MK-8722 at indicated
238 concentration or D2 only were added for another 24h. Lysosomes were then stained with 5 nM
239 Lysotracker RED DND-99 (ThermoFischer L7528) in DMEM for 30 min following the manufacturer
240 instructions. Cells were then detached with trypsin 0.05% for 10 min, transferred into round bottom
241 96well-plate, stained for viability and fixed with PBS-4% PFA. After 20 min, cells were washed and the
242 mean intensity of Lysotracker staining was quantified by flow cytometry as described above.

243

244 **Evaluation of MK-8722 treatment on T cell activation**

245 CD14-depleted PBMCs were thawed and cultured overnight at 37°C in R10 supplemented with 10 UI/mL
246 IL-2 and 1 µg/mL DNAse (StemCell, 07900). Cells were then washed, resuspend cells in R10 and
247 distributed at 10^5 cells/well in a round bottom 96-well plate. Transact stimulation, which is a
248 combination of activating anti-CD3 and anti-CD28 antibodies (Miltenyi, 130-111-160), consisted in 100-
249 fold final dilution of Transact in R10. Alternatively, Spike or Nucleocapsid Peptivator, T cell epitope
250 peptide pools from either Spike or Nucleocapsid of SARS-CoV-2, respectively (Miltenyi 130-126-700 and
251 130-126-698, respectively) was used as stimulation source at a final concentration of 500 ng/mL in R10.
252 After stimulation for 30 min, Brefeldin A (5 µg/mL final) containing anti-CD107a-PE-Cy5 antibody (BD
253 555802) following the manufacturer instruction was added and cells were incubated for 6h. Cells were
254 then washed and stained with anti-CD3-APC-H7 (BD 560176) and anti-CD4-APC (BD 551980) following
255 manufacturer instructions for 10 min on ice, followed by viability staining as described above and
256 fixation in PBS-4% PFA. Cells were further stained overnight with anti-IFNγ-PE (Miltenyi, 130-113-498)
257 following manufacturer instructions in Perm Buffer. Cells were washed in Perm Buffer and then in PBS.
258 Frequencies of $CD4^+$ and $CD8^+$ T cells expressing $CD107a^+$ or $IFN\gamma^+$ were quantified by flow cytometry as

259 described above. For each donor, we determined the net activation (NA) level for each marker after
260 stimulation with Peptivator (NA(Peptivator)) by normalizing CD107a and IFNγ frequencies measured
261 after stimulation with Peptivator over those measured after stimulation with Transact. This activation
262 index reflects the capacity of the donor cells to respond to peptide-specific stimulation relative to its
263 intrinsic stimulatory capacities.

264

265 **Evaluation of combined antiviral effects of MK-8722 and $CD8^+$ T cells from vaccinated individuals on**
266 **epithelial cell infection**

267 $CD8^+$ T cell activation being restricted to MHC-I, antigenic presentation occurs only between as antigen
268 presenting cell (i.e. infected cell) and the T cells with similar HLA. We first showed that Caco2 cells,
269 unlike Calu-3 cells, express the MHC-I molecule HLA-A2 and were thus capable of presenting antigens to
270 HLA-A2-restricted CD8+ T cells from vaccinated individuals. Therefore, confluent Caco2 cells were
271 inoculated for 1h with SARS-CoV-2 and further incubated for 8h in the absence of virus. Previously
272 amplified $CD8^+$ T cells were thawed in R10 complemented with 5IU/mL IL-2 to promote T cell survival,
273 washed and added to Caco2 cells at 8hpi with or without 2.5 or 5 µM MK-8722. The co-cultures were
274 further incubated at 37°C for 36h. T cells were then collected, stained with anti-CD3-APC-H7 (BD
275 560176) and anti-CD8-APC (BD 345775) following manufacturer instructions, and for viability before
276 fixation as above. Cells were then intracellularly stained with anti-spike-AF488 (R&D FAB105403G) for 1h
277 at room temperature. Infection was monitored in $CD3^-CD8^-$ cells by flow cytometry as described above.

278

279 **Graphical representation and statistics**

280 Data and graphs were computed using Graphpad Prism (San Diego, V8). If variables followed a normal
281 distribution after Shapiro-Wilk, *t*-test or ANOVA was calculated; otherwise, statistical analyses were
282 performed using the Mann-Whitney or Kruskal-Wallis test. *p*-values <0.05 were considered significant.
283 Tests were paired when experience design permitted.

284

285 **RESULTS**

286 ***MK-8722 inhibits SARS-CoV-2 replication in epithelial cells.***

287 We first evaluated the activity of the pan-AMPK allosteric activator MK-8722 in Vero76 cells. As early as
288 1h after treatment, MK-7288 activated AMPK and triggered downstream phosphorylation of ACC in a
289 concentration dependent manner from 0.01 to 1 µM (**Fig. S1**). The antiviral activity of MK-8722 was then
290 monitored in Vero76 cells infected by SARS-CoV-2 as schematized (**Fig. 1A**). The drug was added at 0.01
291 to 1 µM to the cells 1h before infection, during the inoculation with SARS-CoV-2 Alpha for 2h, and during
292 the subsequent 24h chase. At 1dpi, Spike expression was quantified by flow cytometry (see gating
293 strategy **Fig. S2A**). Spike$^+$ cell frequency decreased in the presence of MK-8722, from 11.8±0.7% in
294 untreated to 5±0.4% in 1 µM-treated conditions (ANOVA: $p<0.001$, **Fig. S2B**), corresponding to an
295 inhibition of infection of 53±3% at 1 µM (ANOVA: $p<0.0001$, **Fig. 1B**). MK-8722 antiviral activity was
296 further analysed in bronchial Calu-3 cells (See gating strategy **Fig. S2C**), which express TMPRSS2 and are
297 competent for IFN-I signalling similar to bronchial cells *in vivo* unlike Vero76 cells. Infection of Calu-3
298 cells with alpha variant in the presence of MK-8722 significantly decreased the frequency of viral Spike$^+$
299 and viral RNA$^+$ cells in a dose-dependent manner compared to untreated cells (**Fig. S2D**). At 10 µM MK-
300 8722, the frequency of Spike$^+$ and viral RNA$^+$ cells decreased compared to untreated cells, from
301 30.8±2.5% to 3.6±0.2%, and from 15.1±1% to 1.5±0.2%, respectively (ANOVA: $p<0.0001$, **Fig. S2D**). MK-
302 8722 similarly inhibited Omicron infection, the frequency of Spike$^+$ and viral RNA$^+$ cells decreasing

303 compared to untreated cells (compare 27.5±3% versus 4.5±0.6% Spike+ cell frequency and 31±3% vs
304 4.5±0.4% RNA+ cell frequency at 10 µM and without MK-8722, respectively) (**Fig. S2E**). These reductions
305 were comparable to that induced by treating Calu-3 cells with the RNA-dependent RNA polymerase
306 inhibitor Remdesivir at 1 µM (**Fig. S2F**). The IC50 of MK-8722 in Calu-3 cells against Alpha variant was
307 reached at 0.5 µM and an IC90 at 9 µM (*t*-test: $p<0.05$, **Fig. 1C**). For the Omicron variant, MK-8827
308 showed an IC50 at 2 µM and an IC90 slightly above 10 µM (ANOVA: $p<0.05$, **Fig. 1D**). Both RNA^+ and
309 $Spike^+$ frequencies decreased after MK-8722 treatment. As MK-8722 antiviral activity against Alpha and
310 Omicron variants is similar, the drug likely targets the same pathways in the two cases. Furthermore,
311 MK-8722 blocked viral production by Calu-3 cells in a concentration-dependent manner, as quantified by
312 the decrease in *N* RNA by RT-qPCR from $1.5\pm0.14\times10^9$ to $6\pm1.4\times10^7$ viral copies/mL at 10 µM MK-8722
313 (ANOVA: $p<0.0001$) (**Fig. 1E**). MK-8722 did not altered the expression of ACE2 in Vero76 and Calu-3 cells,
314 as measured by flow cytometry (**Fig. S2G**), nor impacted cell viability (**Fig. S2H**).

315 We next investigated whether MK-8722 exerts its antiviral effect at the early infection steps. After MK-
316 8722 pre-treatment of Vero76 and Calu-3 cells (at 1µM and 5µM, respectively), cells were inoculated
317 with Alpha or Omicron variants for 1h at 4°C to allow virus attachment. After virus removal, cells were
318 incubated in the presence of the drug at 37°C to synchronize infection. Viral *N* RNA was quantified by
319 RT-qPCR in the cells after a short (1h) or long (24h in Vero76 and 32h in Calu-3 cells) chase times. As
320 control, cells were similarly infected but left untreated. Viral RNA accumulated after 1h chase in the two
321 cell types for the two variants similarly in treated and non-treated conditions, although the drug had
322 tendency to decrease relative *N* RNA levels in a non-significant statistical manner (1±0.12 vs 0.82±0.08
323 for Vero76, 1±0.05 vs 0.91±0.15 and 1±0.1 vs 0.8±0.08 for Alpha and Omicron variants in Calu-3 cells,
324 respectively, *t*-test: ns in all conditions, **Fig. 1F** and **1G**). In contrast and as expected, *N* RNA expression
325 was significantly reduced after a longer chase (1±0.09 vs 0.52±0.12 for Vero76, 1±0.11 vs 0.2±0.04 and
326 1±0.1 vs 0.03±0.003 for Alpha and Omicron variants in Calu-3 cells, respectively, *t*-test $p<0.05$, <0.0001

327 and <0.0001, respectively). These results suggest that MK-8722 has little antiviral effect during the early
328 steps of infection, namely adsorption and fusion, but acts in a mechanism controlling post-entry
329 replication steps.

330

331 ***Post-infection treatment with MK-8722 is sufficient to inhibit SARS-CoV-2 replication.***

332 We next evaluated if MK-8722 was also active on cells after infection (**Fig. 1H**). Post-exposure treatment
333 from 1 to 3dpi efficiently blocked viral replication, quantified by Spike expression, by 36±7% (**Fig. 1I**,
334 ANOVA: $p<0.0001$), although still less than the continuous treatment, which reduced infection by 63±6%
335 (ANOVA: $p<0.0001$). Continuous and post-exposure treatment with MK-8722 (5 µM) resulted in a similar
336 inhibition of viral genomes accumulation of both Omicron and Alpha variants in infected cells (**Fig. 1J**).
337 Indeed, after continuous treatment with MK-8722 for 34h, *N* RNA relative amount decreased
338 significantly by 80±0.04% and by 97±0.7% in Alpha and Omicron infected cells, respectively (*t*-test:
339 $p<0.0001$ for both variants vs untreated cells). Limiting the MK-8722 treatment to the post-exposure
340 phase, namely from 8hpi, decreased *N* RNA relative amount by 75±0.05% and 80±20% in Alpha and
341 Omicron infected cells, respectively (ANOVA: $p<0.0001$ for both Alpha and Omicron variants vs
342 untreated cells). Altogether, these data suggest that post-exposure treatment by MK-8722 is sufficient
343 to inhibit viral infection.

344

345 ***MK-8722-induced AMPK activation triggers autophagy induction and inhibits lipids metabolism to***
346 ***control SARS-CoV-2 replication.***

347 We further examined the mechanism of SARS-CoV-2 inhibition by MK-8722. Therefore, the modification
348 by the drug of the signalling cascade downstream AMPK activation during SARS-CoV-2 infection of

349 Vero76 and Calu-3 cells relative to no treatment was analysed using western blot (**Fig. S3A-B**).
350 Quantification of the western blots relative to non-infected non-treated control condition is shown in
351 **Fig. 2A** and summarized in a heat map in which values were expressed as log2 fold change (Log2(FC))
352 (**Fig. 2B**). As expected, MK-8722 treatment of both Vero76 and Calu-3 cells significantly activated AMPK
353 that became phosphorylated (0.85±0.4 and 1.2±0.3 log2(FC), *t*-test: $p<0.05$ and $p<0.01$, respectively, **Fig.**
354 **2B**). AMPK phosphorylation was comparable in infected and non-infected cells (0.0±0.5 and -0.02±0.3
355 log2(FC), respectively), while MK-8722 treatment stimulated AMPK phosphorylation even more in
356 infected than in non-infected cells (3.1±0.4 and 2.3±0.9 log2(FC), respectively, *t*-test: $p<0.05$ both). As
357 expected, the drug blocked infection as shown by a significant decrease in N protein levels in both
358 Vero76 and Calu-3 cells (-0.88±0.2 and -1.7±0.4 Log2(FC), respectively, *t*-test: $p<0.05$ both, **Fig. 2A-B**).

359 We then monitored ULK1 phosphorylation and p62 relative expression as markers of the initiation of
360 autophagy, Raptor phosphorylation as a marker of protein synthesis inhibition, and ACC phosphorylation
361 as a marker of the disruption of lipid metabolism. While neither MK-8722 nor SARS-CoV-2 infection
362 alone affected ULK1 phosphorylation (with the exception of Calu-3 cells, non-infected but treated,
363 where increase reached 1±0.2 Log2(FC), $p<0.01$), MK-8722 treatment during infection was associated
364 with an increase in ULK1 phosphorylation in both cell types (from 0.05±0.5 to 2.8±1.2 Log2(FC) in Vero76
365 cells and from -0.9±0.5 to 1.3 ±0.6 Log2(FC) in Calu-3 cells, *t*-test: ns and $p<0.05$, respectively, **Fig. 2A-B**).
366 Concomitantly, p62 expression strongly and significantly increased in both cell types (3.33±0.56 and
367 2±0.6 Log2(FC) for Vero76 and Calu-3 cells, respectively, *t*-test $p<0.05$, **Fig. 2A-B**). Raptor
368 phosphorylation remained unchanged whatever the conditions. Finally, SARS-CoV-2 infection strongly
369 decreased ACC phosphorylation significantly (-1±0.29 and -0.7±0.2 Log2(FC), respectively and *t*-test:
370 $p<0.05$, **Fig. 2A-B**) while it was significantly increased by MK-8722 treatment during infection (1.9±0.5
371 and 1±0.2 Log2(FC), *t*-test: $p<0.05$ and $p<0.01$, respectively, **Fig. 2A-B**).

372 Altogether these results suggest that the antiviral mechanism of MK-8722 relies on the AMPK activation-
373 dependent restoration of the autophagic flux that is otherwise blocked by SARS-CoV-2 proteins, due to
374 ULK1. Phosphorylation of ULK1 and increased p62 expression likely result in an increased access of viral
375 components to phagosomes and further phagosomes fusion with lysosomes, resulting in subsequent
376 degradation of viral proteins in phagolysosomes, preventing viral dissemination. As complementary anti-
377 viral mechanism, MK-8722 treatment increases ACC phosphorylation that decreases lipid synthesis,
378 which may reduce lipid droplets content and thus affect the establishment of viral factories. However,
379 as shown by the lack of Raptor phosphorylation, the antiviral activity of MK-8722 does not involve a
380 shutdown of viral protein synthesis.

381

382 ***MK-8722 treatment perturbs the viral factory establishment.***

383 We next explored the capacity of MK-8722 to perturb the distribution of lipids associated with viral
384 factories and lipid droplets in cells infected with the Alpha variant. Therefore, lipid reorganisation in
385 infected Calu-3 cells was monitored after continuous treatment with MK-8722 by staining lipids with the
386 lipophilic marker Nile Red analysed by confocal microscopy. As expected [32], treatment with MK-8722 in
387 uninfected cells blocked almost entirely the synthesis of lipids, as shown by the loss of Nile Red staining
388 (**Fig. S4A**). Infection increased the overall Nile Red staining by 40±10% compared to non-infected cells
389 (**Fig. S4B**, ANOVA: $p<0.05$), but also dramatically modified Nile Red cellular distribution into aggregates
390 likely corresponding to lipid droplets (compare **Fig. 3A,-S4B**). This overall infection-induced increase in
391 Nile Red staining was abolished by MK-8722 treatment (**Fig. S4B**, 0.943±0.14-fold change, infected non-
392 treated vs treated cells, ANOVA: $p<0.05$) and returned to untreated uninfected cell level. Furthermore,
393 in infected cell, identified by viral N protein labelling, MK-8722 significantly reduced the number, area
394 and intensity of lipids droplets (as defined in the method section) (**Fig. 3A** and **3B**, 0.29±0.09 and

395 0.28±0.1 and 0.33±0.15 fold-change over infected non-treated cells, *t*-test: $p<0.01$, $p<0.05$ and $p<0.05$,
396 respectively). We then evaluated if the N protein, a maker of virus replication in viral factories, was
397 redistributed out of lipid droplets by the drug. In the absence of MK-treatment, N protein and lipids
398 colocalized as expected, although partially, with Manders' Overlap Coefficient (MOC) being in the range
399 of previous reports [12]. This colocalisation decreased significantly in cells infected in the presence of MK-
400 8722, as indicated by lower MOCs for N protein in Nile Red (0.085±0.024 vs 0.01±0.005, Mann-Whitney
401 $p<0.001$) and for Nile Red in N protein (0.16±0.05 vs 0.027±0.01, Mann-Whitney $p<0.01$) in MK-8722
402 treated vs untreated infected cells (**Fig. 3~~B~~A** and **3C**). Altogether, SARS-CoV-2 infection increases the
403 accumulation of lipid droplets with which viral components colocalise. MK-8722 treatment reverses
404 these effects, likely reflecting an alteration of cell lipid composition following increased ACC
405 phosphorylation, thus limiting the production of viral factories.

406 SARS-CoV-2 is an enveloped virus; therefore lipid metabolism modification alters the lipid composition
407 of the viral membrane, and in turn viral particles infectivity [5,7–11] We thus measured viral production by
408 infected Vero76 and Calu-3 cells by quantification of secreted viral nucleocapsid *N* RNA by RT-qPCR. In
409 line with the reduction of secreted viral *N* RNA in presence of the drug shown above (**Fig. 1E**), the level
410 of viral *N* RNA secreted by both infected cell lines was reduced by 10-fold upon continuous MK-8722
411 treatment (**Fig. 3D**, $2\pm0.8\times10^4$ vs $6\pm2\times10^2$ and $3.4\pm1.7\times10^7$ vs $2.3\pm1.2\times10^6$ RNA copies/mL for Vero
412 (upper) and Calu-3 cells (lower), respectively, *t*-test: $p<0.05$ for Vero76 and $p<0.01$ for Calu-3 cells).
413 Accordingly, the amount of infectious viruses released by infected cells titrated in foci forming assay was
414 statistically decreased by MK-8722 in Vero76 (from $3\pm0.3\times10^4$ to $5.8\pm1\times10^3$ FFU/mL) and Calu-3 cells
415 (from $2.6\pm0.5\times10^5$ to $5.5\pm1\times10^4$ FFU/mL, *t*-test: $p<0.05$ for both cell types, **Fig. 3E**).

416 We next calculated an infectious index of released particles (described in the method section), which
417 inversely correlates with virus infectivity. The drug reduced the frequency of newly produced infectious
418 viruses by both cell lines (infectious index: 0.41±0.11 vs 0.05±0.02 in Vero76 cells (Mann-Whitney

419 $p<0.05$), and 0.07±0.03 vs 0.007±0.003 in Calu-3 cells (Mann-Whitney $p<0.05$) in the presence and
420 absence of the drug) (The drug reduced the frequency of newly produced infectious viruses by both cell
421 lines **Fig. 3F**). This inhibitory effect of MK-8722 on the production of infectious particles could not be
422 explained by a direct inhibitory role of MK-8722 present in the culture media on foci formation. Indeed,
423 tested cell culture media (**Fig. 1B, S2B**) were highly diluted in the assay (at least 1,000 times)
424 corresponding to a MK-8722 concentration < 0.005 µM, which is far under the limit of efficacy of MK-
425 8722 in Vero76 cells. Furthermore, MK-8722 exposure was limited to the 2h inoculation. Our data
426 suggests that the lipid metabolism alteration induced by MK-8722 counteracts SARS-CoV-2 replication
427 and affects production and infectivity of released viral particles.

428

429 ***MK-8722 enhances lysosomal degradation of viral components to promote antiviral immunity.***

430 As antiviral mechanism, MK-8722 could contribute to restoration of the autophagic flux (**Fig. 2**), which
431 should result in targeting viral proteins to lysosomes. We first evaluated the lysosome distribution after
432 MK-8722 treatment in infected cells. As a lysosomal marker, we used LAMP1 and characterized its
433 distribution in infected Calu-3 cells upon MK-8722 treatment by immunolabelling and confocal
434 microscopy in infected (**Fig. 4A**) and non-infected cells (**Fig. S5A**). SARS-CoV-2 infection significantly
435 decreased LAMP1 relative expression in Calu-3 cells as expected (**Fig. 4A and S5A,** quantified in **Fig. S5B**
436 as 0.47±0.06-fold change, ANOVA: $p<0.05$). This decrease likely reduced $LAMP1^+$ lysosome size as
437 infection inhibits autophagosome-lysosome fusion[19,21,22]. MK-8722 treatment during infection
438 significantly restored LAMP1 relative expression to its level in non-infected non-treated condition
439 (1.15±0.11-fold change, ANOVA: $p<0.01$ compared to infected non-treated condition; **Fig. S5B**).

440 We then characterized $LAMP1^+$ lysosome parameters, as defined in the method section. MK-8722
441 significantly increased $LAMP1^+$ lysosome number, area and specific intensity, indicative of their

442 enhanced activity in infected cells, which were identified by the expression of viral N protein (**Fig. 4B**,
443 2.5±0.25 and 2.53±0.2 and 4.3±1.1-fold change over infected non-treated cells, *t*-test: $p<0.001$, $p<0.05$
444 and $p<0.0001$, respectively). When colocalization of viral N protein and LAMP1 was quantified in
445 infected cells, MK-8722 treatment resulted in higher MOC as compared to infected non-treated cells (N
446 protein in LAMP1 signal: 0.02±0.003 vs 0.05±0.004, Mann-Whitney $p<0.01$; and LAMP1 in N protein
447 signal: 0.021±0.006 vs 0.048±0.007, Mann-Whitney $p<0.05$, **Fig. 4C**). Lysosomal activity was quantified
448 after Lysotracker staining by flow cytometry in Calu-3 cells infected for 24h and treated with MK-8722
449 for an additional day. MK-8722 increased lysosomal activity similarly after infection by both Alpha and
450 Omicron variants (Lysotracker MFI: 286±12 and 289±9.6 in MK-8722 treated vs 253±34 and 251±6 in
451 non-treated cells, respectively for each variant, ANOVA: $p<0.05$ at least, **Fig. 4D**). Altogether in infected
452 cells, MK-8722 treatment increases lysosomal activity and addresses viral components to the lysosome,
453 likely for degradation.

454

455 **MK-8722 restores the INF I pathway**

456 The lack of type-I IFN response is a major immune parameter contributing to COVID19 disease [27,39,40].
457 Completion of autophagy will most likely result in the degradation of viral proteins, which escape RIG-I
458 sensing thereby restoring IFNα and IFNβ production and associated downstream ISG such as *OAS1* and
459 *Mx1*. We thus investigated IFN-I response in infected Calu-3 cells after continuous or post-infection
460 treatment with MK-8722 (**Fig. 4E**). Compared to untreated condition, continuous and post-infection
461 treatment with MK-8722 increased *IFNα* mRNA expression by 100±38% and 140±58% (Kruskal-Wallis:
462 $p<0.05$ for both treatments), while that of *IFNβ* decreased by 73±5% and 45±11% for continuous and
463 post-infection treatment, respectively (Kruskall-Wallis: $p<0.01$ and ns respectively). Regarding *ISG* mRNA
464 expression, *Mx1* level increased by 1.46±0.12-fold and by 1.49±0.19-fold for continuous and post-

465 infection treatment, respectively (Kruskal-Wallis: <0.05 both, respectively), while *OAS1* mRNA
466 expression increased by more than 2-fold in all treated conditions (2.8±0.6-fold and 2.1±0.3-fold,
467 respectively, Kruskal-Wallis: $p<0.01$). Altogether, MK-8722 treatment, even if initiated post-exposure,
468 can drive early IFN-I expression and downstream ISG, which, by controlling infection, could limit severe
469 outcome in patients [24,25,27,39,41].

470

471 **MK-8722 *in vitro* treatment does not alter T cell response against SARS-CoV-2 in vaccinated individuals**

472 T cell response is crucial to control SARS-CoV-2 infection [42–44], and relies on metabolism reprogramming
473 of the effector cell. We therefore investigated the impact of MK-8722-mediated AMPK activation on the
474 T cell response. We found that MK-8722 alone compared to DMSO at identical concentration did not
475 activate T-cell from healthy donors (**Fig. S6A-B**). We then investigated if MK-8722 exposure affected T
476 cell responses upon TCR engagement. Healthy donor PBMCs were stimulated with anti-CD3 and anti-
477 CD28 (CD3/CD28, TransAct) to mimicking TCR engagement, and treated with MK-8722 for 6h.
478 Intracellular IFNγ$^+$ and CD107a$^+$ frequencies were then analysed in CD4$^+$ and CD8$^+$ T cells. As expected,
479 CD3/CD28 stimulation increased both IFNγ$^+$ and CD107a$^+$ frequencies in both CD4$^+$ and CD8$^+$ T cells (**Fig.
480 5A**, 5.6±1.5% and 7.5±1.9% vs 0.6±0.2% and 1.1±0.2% for CD4$^+$ T cells, and 4.9±1.5% and 2±0.3% vs
481 0.68±0.1% and 0.3±0.06% for CD8$^+$ T cells, for IFNγ$^+$ and CD107a$^+$ frequencies respectively, *t*-test: $p<0.05$
482 at least). The concentrations of MK-8722 tested had no negative impact on the expression of activation
483 markers, and even showed a trend towards increased activation with MK-8722 treatment. These results
484 indicate that MK-8722 does not affect degranulation and IFNγ responses and is thus compatible with the
485 establishment of a T cell-dependent protective immune response.

486 We next tested whether MK-8722 altered antigen-specific T cell stimulation. As a surrogate of SARS-
487 CoV-2 antigen, we used peptides covering the immunodominant sequence domains of the SARS-CoV-2

488 Spike (Peptivator peptide pool (Miltenyi)) to stimulate CD14-depleted PBMCs. We defined an activation
489 index as the level of activation induced by the peptide pool relative to the corresponding Transact level.
490 For these experiments, cells were collected from healthy individuals after summer 2021 when most of
491 them had been immunized at least two times with spike-based SARS-Cov-2 vaccine and consequently
492 mounted a Spike-specific T cell response. Accordingly, Spike peptides stimulated only $CD4^+$ T cell
493 response although in a limited manner (**Fig. 5B**, activation index: 6.6±0.8 for IFNγ and 1.4±0.3 for
494 CD107a, *t-test:* $p<0.01$ and $p<0.05$). As for CD3/CD28 stimulation, MK-8722 stimulation showed a trend
495 towards increase all the tested T cell responses although only CD107a activation index for CD4+ T-cells
496 was statistically higher afer MK-8722 treatment (i.e. 6.6±0.8 vs 13.3±4.7 for 10 µM MK-8722, ANOVA
497 $p<0.01$). Stimulation of CD14-depleted PBMCs with a SARS-CoV-2 Nucleocapsid peptide pool gave similar
498 results, even though the peptide pool alone failed to activate a T cell response (**Fig. S6C**). These data
499 suggests that if used as a drug, MK-8722 will likely not prevent the establishment of a T cell- specific
500 response against SARS-CoV-2 *in vivo*.

501 We finally evaluated whether MK-8722 and SARS-CoV-2-specific $CD8^+$ T cells could cooperate to block
502 infection of mucosal epithelial Caco2 cells, which expressed HLA-A2 (not shown). Therefore, $CD8^+$ T cells
503 were obtained from HLA-$A2^+$ healthy donors obtained after the summer 2021. Post-exposure treatment
504 with MK-8722 inhibited infection of Caco2 cells in a dose dependent manner (by 32±3% and 54±6%, at
505 2.5 and 5 µM respectively (ANOVA: $p<0.0001$ for both conditions, see **Fig. S7** for the gating strategy). In
506 the presence of $CD8^+$ T cells, infection of Caco2 cells was reduced by 19.8±5% (ANOVA: $p<0.01$).
507 Moreover, the combination of $CD8^+$ T cells with MK-8722 increased the inhibition of infection in a dose-
508 dependent manner (50±3% and 71±4% inhibition in the presence of CD8+ T cells and 2.5 or 5 µM MK-
509 8722, respectively) compared to the inhibition of infection in the sole presence of CD8+ T cells (19.8±5%
510 ANOVA: $p<0.0001$ both, respectively) and in the presence of MK-8722 only (32±3% and 54±6% in the
511 presence of 2.5 or 5 µM MK-8722, *t*-test $p<0.05$ and ns for 2.5 and 5 µM, respectively) although no

512 synergy was observed. Altogether, our results confirm that MK-8722 treatment does not impair the
513 SARS-CoV-2-specific $CD8^+$ T cell-mediated response against mucosal Caco2 cell infection, but rather that
514 both act in combination to reduce cell infection.

515

516 **DISCUSSION**

517 To date, antivirals against SARS-CoV-2 infection without significant side effects have yet to be
518 characterised. Here, we provide evidence that the direct pan-AMPK allosteric activator MK-8722 is a
519 strong antiviral drug candidate against SARS-CoV-2 infection, as treatment with MK-8722 in the µM
520 range reduces infection of lung cells without altering the cellular immune response.

521 Previous studies have suggested that AMPK activation could inhibit viral infections [32], as viral infection
522 prevents AMPK activity. In the case of SARS-CoV-2 infection, AMPK activity is reduced and furthermore,
523 autophagy is blocked [45], while inhibition of either AMPK by Compound C or ULK1 by MRT68921
524 increases viral particle release [45,46]. Conversely, we show here that pharmacological allosteric pan-
525 activation of AMPK with MK-8722 at µM concentration blocks infection. In line, metformin, a drug
526 approved by FDA since 1994, and the adenosine analogue AICAR that activates AMPK indirectly can
527 inhibit replication of SARS-CoV-2 as well as *Flaviviruses*, but at concentrations above 10 and 1 mM,
528 respectively [45,46]. These AMPK-sensitive viruses replicate all in viral factories, disturbing lipid synthesis
529 and escaping autophagy [47,48].

530 Despite observational data suggesting an association between metformin use and prevention of severe
531 COVID-19 outcomes, metformin did not significantly lower risk of hospitalization and mortality due to
532 SARS-CoV2 infection in recent randomized controlled trials [49]. Furthermore, *in vivo*, metformin mainly
533 targets the liver and the gastrointestinal tract [50] and therefore could have limited effect in the upper
534 airway, the SARS-CoV-2 infection site. In contrast, MK-8722 may reach these tissues with minimal side

535 effects, as a daily treatment in diabetic Non-human primates (NHPs) with MK-8722 (10 mg/kg) for a
536 month induced only a limited and reversible cardiac hypertrophy [34]. The MK-8722 antiviral treatment we
537 report is efficient *in vitro* not only when applied from the onset of infection but also after infection.
538 Therefore, MK-8722 might be tested as post-exposure prophylaxis against SARS-CoV-2, thereby limiting
539 potential severe outcomes.

540

541 Mechanistically, we demonstrated here that AMPK activation by MK-8722 reduces lipid synthesis
542 through the inhibition of ACC by acting on the limiting step of fatty acid production and, consequently,
543 of phospholipid synthesis. This inhibition leads to a reduction in the formation of lipid droplets and a
544 significant reduction in the infectivity of viral particles. Lipid synthesis is required to extend endoplasmic
545 reticulum for the genesis of the viral factories and to generate the viral membrane of SARS-CoV-2, which
546 is an enveloped virus. Changes in lipid content of viral particles have been shown to impact infectivity
547 [5,7,9,11]. AMPK-mediated inhibition of ACC by MK-8722 treatment likely modifies all membrane lipid
548 species in SARS-CoV-2 infected cells [51], in turn affecting viral membrane lipid composition and likely the
549 lower virus infectivity we observed. The modification of the cellular lipid content by MK-8722 treatment
550 might also block the release of pro-inflammatory molecules otherwise induced by infection, such as IL-6
551 and LTB4 [12,52]. SARS-CoV-2 affects also cholesterol metabolism [7,53,54] and patients under statins who
552 contracted SARS-CoV-2 developed better T cell responses and showed lower grade of pulmonary
553 symptoms [55,56]. AMPK activation also inhibits HMG-CoA-reductase, the major enzyme for cholesterol
554 synthesis. MK-8722 treatment might therefore be beneficial for COVID-19 patients through multiple
555 mechanisms [7,14,17]. The molecular mechanisms underlying the changes in the lipid spectrum and
556 cholesterol content in infected cells following treatment with MK-8722 remain to be understood.

557 Increased activation of ULK1 and expression of Sequestosome-1/p62 upon MK-8722 treatment *in vitro*
558 reflects a restoration of the autophagy flux and the targeting of viruses to lysosome for degradation.
559 This mechanism is otherwise blocked by viral replication in an ORF3- and ORF7a-mediated process,
560 which inhibits HOPS complex-mediated assembly of the SNARE complex required for autolysosome
561 formation [19,21,22]. Sequestrosome-1/p62 is an autophagy cargo receptor that plays a key role in
562 mediating the formation of autophagosomes and autophagic clearance of intracellular protein
563 aggregates by its binding to LC3b. A modification of p62 expression and LC3b binding capacity upon
564 SARS-CoV-2 infection has been observed *in vitro* [19,22,57]. Together, these data suggest that SARS-CoV-2-
565 mediated disruption of p62 expression and/or function impairs fusion of phagosome with lysosome [19,57–
566 59]. The increased p62 expression we observed upon MK-8722 treatment together with the increased
567 ULK1 activation will likely result in p62 activation, in turn promoting phagolysosomes formation as we
568 reported**.** P62 also induces proteasomal degradation[60], and its increased expression could contribute in
569 the antiviral activity of MK-8722.

570 The restoration of autophagy by MK-8722 we report, and thereby degradation of viral components, will
571 improve MHC-I presentation and the cellular cytotoxic response [61], contributing to the therapeutic value
572 of MK-8722 treatment. Furthermore, defective viral particles, which are produced upon MK-8722
573 treatment, might be detected by innate immune sensors such as MAVS [62], promoting a type-I IFN
574 response and protection from SARS-CoV-2 infection [26]. MK-8722 treatment of infected cells also unlocks
575 the IFN-I response, as shown by the increase in *IFNα* and both ISG *Mx1* and *OAS1* mRNA we observed.
576 This IFN-I response most likely associates with a better control of infection and lowers pathology score
577 [24,25,27,39,63]. The induction of IFNβ by poly I:C is only transient, with its mRNA returning even to a level
578 below the basal one [64]. Here, continuous but not post infection treatment with MK-8722 may similarly
579 result in a transient accumulation of *IFNβ* mRNA, the final level of which is statistically lower than that
580 observed in the absence of treatment. This faster IFN-I response could enhance protection of individuals

581 against SARS-CoV-2, since a delay in IFN-I response is associated with disease severity [27,39] and post
582 infection treatment of severe COVID with IFNα2b significantly improved patient outcome [40].

583 Finally, MK-8722 could also enhance the response of SARS-CoV-2-specific $CD8^+$ T cells at the site of
584 infection which is crucial for protection in NHP and in humans [42–44]. Optimal $CD8^+$ T cells responses at
585 mucosal level can be boosted by IFN-I, which showed vaccine adjuvant-like properties in strategies
586 against other infectious diseases and cancer [65–68]. MK-8722 treatment, which stimulates the IFN-I
587 pathway upon infection, as shown here, could therefore contribute to improve the $CD8^+$ T cells
588 response. Accordingly, *in vitro*, MK-8722 does not antagonise but rather slightly enhance the T cell
589 response and when combined with $CD8^+$ T cells, resulting treatment increases inhibition of infection
590 compared to either treatment alone. Further studies on the crosstalk between $CD8^+$ T cells, phagocyte
591 and infected epithelial cells will clarify how MK-8722 modulates the $CD8^+$ T cell response.

592 In summary, to optimize safely antiviral treatment against SARS-CoV-2, we propose here to target the
593 energy sensor AMPK using small molecule pan-AMPK allosteric activators (such as MK-8722), rather
594 than targeting the virus itself. The antiviral mechanism of MK-8722 relies on the reversion of three
595 major pathways affected by SARS-CoV-2 infection, namely lipid metabolism, autophagy and IFN-I
596 response. Therefore, to escape MK-8722 and generate resistant and more pathogenic variants, SARS-
597 CoV-2 will need to acquire a higher number of resistance mutations than a drug targeting on a single
598 pathway. Furthermore, by increasing the SARS-CoV-2 $CD8^+$ T cell response, MK-8722 treatment would
599 result in a faster response against infection and better outcome. *Coronaviruses* but also *Flaviviruses*
600 replicate within viral factories and/or disturb lipid metabolism, hijack autophagy and IFN-I response. We
601 therefore propose that MK-8722 could act as antiviral against other *Coronaviruses* and *Flaviviruses*,
602 ensuring a larger available therapeutic arsenal against future emerging virosis.

603

604 ## References

605 1. Fernandes, Q. *et al.* Emerging COVID-19 variants and their impact on SARS-CoV-2 diagnosis,
606 therapeutics and vaccines. *Ann Med* **54**, 524–540 (2022).
607 2. Haque, Ashwaq, O., Sarief, A. & Azad John Mohamed, A. K. A comprehensive review about SARS-
608 CoV-2. *Future Virol* **15**, 625–648 (2020).
609 3. Ji, M. *et al.* VMP1 and TMEM41B are essential for DMV formation during β-coronavirus infection. *J*
610 *Cell Biol* **221**, e202112081 (2022).
611 4. Snijder, E. J. *et al.* A unifying structural and functional model of the coronavirus replication
612 organelle: Tracking down RNA synthesis. *PLOS Biology* **18**, e3000715 (2020).
613 5. Farley, S. E. *et al.* A global lipid map reveals host dependency factors conserved across SARS-CoV-2
614 variants. *Nat Commun* **13**, 3487 (2022).
615 6. Tabata, K. *et al.* Convergent use of phosphatidic acid for hepatitis C virus and SARS-CoV-2 replication
616 organelle formation. *Nat Commun* **12**, 7276 (2021).
617 7. Tanner, J. E. & Alfieri, C. The Fatty Acid Lipid Metabolism Nexus in COVID-19. *Viruses* **13**, 90 (2021).
618 8. Bajimaya, S., Frankl, T., Hayashi, T. & Takimoto, T. Cholesterol is required for stability and infectivity
619 of influenza A and respiratory syncytial viruses. *Virology* **510**, 234–241 (2017).
620 9. Cheng, N. *et al.* Protein post-translational modification in SARS-CoV-2 and host interaction. *Front*
621 *Immunol* **13**, 1068449 (2022).
622 10. McBride, C. E. & Machamer, C. E. Palmitoylation of SARS-CoV S protein is necessary for partitioning
623 into detergent-resistant membranes and cell–cell fusion but not interaction with M protein.
624 *Virology* **405**, 139–148 (2010).
625 11. Mesquita, F. S. *et al.* S-acylation controls SARS-CoV-2 membrane lipid organization and enhances
626 infectivity. *Dev Cell* **56**, 2790-2807.e8 (2021).

627 12. Dias, S. S. G. *et al.* Lipid droplets fuel SARS-CoV-2 replication and production of inflammatory
628 mediators. *PLoS Pathog* **16**, e1009127 (2020).
629 13. Grootemaat, A. E. *et al.* Lipid and Nucleocapsid N-Protein Accumulation in COVID-19 Patient Lung
630 and Infected Cells. *Microbiology Spectrum* **10**, e01271-21 (2022).
631 14. Nardacci, R. *et al.* Evidences for lipid involvement in SARS-CoV-2 cytopathogenesis. *Cell Death Dis*
632 **12**, 1–12 (2021).
633 15. Wang, W. *et al.* Genetic variety of ORF3a shapes SARS-CoV-2 fitness through modulation of lipid
634 droplet. *J Med Virol* **95**, e28630 (2023).
635 16. Chu, J. *et al.* Pharmacological inhibition of fatty acid synthesis blocks SARS-CoV-2 replication. *Nat*
636 *Metab* **3**, 1466–1475 (2021).
637 17. Koepke, L., Hirschenberger, M., Hayn, M., Kirchhoff, F. & Sparrer, K. M. Manipulation of autophagy
638 by SARS-CoV-2 proteins. *Autophagy* **17**, 2659–2661 (2021).
639 18. Twu, W.-I. *et al.* Contribution of autophagy machinery factors to HCV and SARS-CoV-2 replication
640 organelle formation. *Cell Rep* **37**, 110049 (2021).
641 19. Hou, P. *et al.* The ORF7a protein of SARS-CoV-2 initiates autophagy and limits autophagosome-
642 lysosome fusion via degradation of SNAP29 to promote virus replication. *Autophagy* **19**, 551–569
643 (2023).
644 20. Koyama-Honda, I., Itakura, E., Fujiwara, T. K. & Mizushima, N. Temporal analysis of recruitment of
645 mammalian ATG proteins to the autophagosome formation site. *Autophagy* **9**, 1491–1499 (2013).
646 21. Miao, G. *et al.* ORF3a of the COVID-19 virus SARS-CoV-2 blocks HOPS complex-mediated assembly of
647 the SNARE complex required for autolysosome formation. *Dev Cell* **56**, 427-442.e5 (2021).
648 22. Zhang *et al.* The SARS-CoV-2 protein ORF3a inhibits fusion of autophagosomes with lysosomes. *Cell*
649 *Discov* **7**, 31 (2021).

650 23. Zhou, H., Hu, Z. & Castro-Gonzalez, S. Bidirectional interplay between SARS-CoV-2 and autophagy.
651 *mBio* **0**, e01020-23 (2023).
652 24. Bizzotto, J. *et al.* SARS-CoV-2 Infection Boosts MX1 Antiviral Effector in COVID-19 Patients. *iScience*
653 **23**, 101585 (2020).
654 25. Danziger, O., Patel, R. S., DeGrace, E. J., Rosen, M. R. & Rosenberg, B. R. Inducible CRISPR activation
655 screen for interferon-stimulated genes identifies OAS1 as a SARS-CoV-2 restriction factor. *PLOS*
656 *Pathogens* **18**, e1010464 (2022).
657 26. Li, X. *et al.* SARS-CoV-2 ORF10 suppresses the antiviral innate immune response by degrading MAVS
658 through mitophagy. *Cell Mol Immunol* **19**, 67–78 (2022).
659 27. Smith, N. *et al.* Defective activation and regulation of type I interferon immunity is associated with
660 increasing COVID-19 severity. *Nat Commun* **13**, 7254 (2022).
661 28. Øynebråten, I. Involvement of autophagy in MHC class I antigen presentation. *Scand J Immunol* **92**,
662 e12978 (2020).
663 29. Wen, Z. *et al.* Enhancement of SARS-CoV-2 N Antigen-Specific T Cell Functionality by Modulating the
664 Autophagy-Mediated Signal Pathway in Mice. *Viruses* **15**, 1316 (2023).
665 30. Zhang *et al.* The ORF8 protein of SARS-CoV-2 mediates immune evasion through down-regulating
666 MHC-I. *Proc Natl Acad Sci U S A* **118**, e2024202118 (2021).
667 31. Steinberg, G. R. & Hardie, D. G. New insights into activation and function of the AMPK. *Nat Rev Mol*
668 *Cell Biol* **24**, 255–272 (2023).
669 32. Moreira, D. *et al.* AMP-activated protein kinase as a target for pathogens: friends or foes? *Curr Drug*
670 *Targets* **17**, 942–953 (2016).
671 33. Farfan-Morales, C. N. *et al.* The antiviral effect of metformin on zika and dengue virus infection. *Sci*
672 *Rep* **11**, 8743 (2021).

673 34. Myers, R. W. *et al.* Systemic pan-AMPK activator MK-8722 improves glucose homeostasis but
674 induces cardiac hypertrophy. *Science* **357**, 507–511 (2017).
675 35. Muise, E. S. *et al.* Pharmacological AMPK activation induces transcriptional responses congruent to
676 exercise in skeletal and cardiac muscle, adipose tissues and liver. *PLOS ONE* **14**, e0211568 (2019).
677 36. Cottignies-Calamarte, A., He, F., Zhu, A., Real, F. & Bomsel, M. Protocol to detect infectious SARS-
678 CoV-2 at low levels using in situ hybridization techniques. *STAR Protocols* **4**, 102593 (2023).
679 37. Desmarets, L. *et al.* A reporter cell line for the automated quantification of SARS-CoV-2 infection in
680 living cells. *Front Microbiol* **13**, 1031204 (2022).
681 38. Lu, X. *et al.* US CDC Real-Time Reverse Transcription PCR Panel for Detection of Severe Acute
682 Respiratory Syndrome Coronavirus 2. *Emerg Infect Dis* **26**, 1654–1665 (2020).
683 39. Decker, T. The early interferon catches the SARS-CoV-2. *Journal of Experimental Medicine* **218**,
684 e20211667 (2021).
685 40. Zhou, Q. *et al.* Interferon-α2b Treatment for COVID-19. *Front Immunol* **11**, 1061 (2020).
686 41. Schroeder, S. *et al.* Interferon antagonism by SARS-CoV-2: a functional study using reverse genetics.
687 *The Lancet Microbe* **2**, e210–e218 (2021).
688 42. Liu, J. *et al.* CD8 T cells contribute to vaccine protection against SARS-CoV-2 in macaques. *Sci*
689 *Immunol* **7**, eabq7647 (2022).
690 43. Taus, E. *et al.* Dominant CD8+ T Cell Nucleocapsid Targeting in SARS-CoV-2 Infection and Broad Spike
691 Targeting From Vaccination. *Front Immunol* **13**, 835830 (2022).
692 44. Vitiello, L. *et al.* Long Lasting Cellular Immune Response Induced by mRNA Vaccination: Implication
693 for Prevention Strategies. *Front Immunol* **13**, 836495 (2022).
694 45. Gassen, N. C. *et al.* SARS-CoV-2-mediated dysregulation of metabolism and autophagy uncovers
695 host-targeting antivirals. *Nat Commun* **12**, 3818 (2021).

696 46. Parthasarathy, H., Tandel, D., Siddiqui, A. H. & Harshan, K. H. Metformin suppresses SARS-CoV-2 in
697 cell culture. *Virus Research* **323**, 199010 (2023).
698 47. Farfan-Morales, C. N. *et al.* Anti-flavivirus Properties of Lipid-Lowering Drugs. *Frontiers in Physiology*
699 **12**, (2021).
700 48. Jiménez de Oya, N., Blázquez, A.-B., Casas, J., Saiz, J.-C. & Martín-Acebes, M. A. Direct Activation of
701 Adenosine Monophosphate-Activated Protein Kinase (AMPK) by PF-06409577 Inhibits Flavivirus
702 Infection through Modification of Host Cell Lipid Metabolism. *Antimicrob Agents Chemother* **62**,
703 e00360-18 (2018).
704 49. Erickson, S. M. *et al.* Metformin for Treatment of Acute COVID-19: Systematic Review of Clinical Trial
705 Data Against SARS-CoV-2. *Diabetes Care* **46**, 1432–1442 (2023).
706 50. Foretz, M., Even, P. C. & Viollet, B. AMPK Activation Reduces Hepatic Lipid Content by Increasing Fat
707 Oxidation In Vivo. *Int J Mol Sci* **19**, E2826 (2018).
708 51. Yeudall, S. *et al.* Macrophage acetyl-CoA carboxylase regulates acute inflammation through control
709 of glucose and lipid metabolism. *Sci Adv* **8**, eabq1984 (2022).
710 52. Fomin, G. *et al.* Cytokine response and damages in the lungs of aging Syrian hamsters on a high-fat
711 diet infected with the SARS-CoV-2 virus. *Front Immunol* **14**, 1223086 (2023).
712 53. Tsai, P.-H. *et al.* Modifications of lipid pathways restrict SARS-CoV-2 propagation in human induced
713 pluripotent stem cell-derived 3D airway organoids. *Journal of Advanced Research* (2023)
714 doi:10.1016/j.jare.2023.08.005.
715 54. Yuan, Y. *et al.* The CH24H metabolite, 24HC, blocks viral entry by disrupting intracellular cholesterol
716 homeostasis. *Redox Biol* **64**, 102769 (2023).
717 55. Santosa, A. *et al.* Protective effects of statins on COVID-19 risk, severity and fatal outcome: a
718 nationwide Swedish cohort study. *Sci Rep* **12**, 12047 (2022).

719 56. Teixeira, L. *et al.* Simvastatin Downregulates the SARS-CoV-2-Induced Inflammatory Response and
720 Impairs Viral Infection Through Disruption of Lipid Rafts. *Front Immunol* **13**, 820131 (2022).
721 57. Zhang, Y., Liu, S., Xu, Q., Li, H. & Lu, K. Cleavage of the selective autophagy receptor SQSTM1/p62 by
722 the SARS-CoV-2 main protease NSP5 prevents the autophagic degradation of viral membrane
723 proteins. *Mol Biomed* **3**, 17 (2022).
724 58. Paunovic, V. *et al.* Autophagy Receptor p62 Regulates SARS-CoV-2-Induced Inflammation in COVID-
725 19. *Cells* **12**, 1282 (2023).
726 59. Tan, X. *et al.* Coronavirus subverts ER-phagy by hijacking FAM134B and ATL3 into p62 condensates
727 to facilitate viral replication. *Cell Rep* **42**, 112286 (2023).
728 60. Kumar, A. V., Mills, J. & Lapierre, L. R. Selective Autophagy Receptor p62/SQSTM1, a Pivotal Player
729 in Stress and Aging. *Frontiers in Cell and Developmental Biology* **10**, (2022).
730 61. Gestal-Mato, U. & Herhaus, L. Autophagy-dependent regulation of MHC-I molecule presentation. *J*
731 *Cell Biochem* (2023) doi:10.1002/jcb.30416.
732 62. Manzoni, T. B. & López, C. B. Defective (interfering) viral genomes re-explored: impact on antiviral
733 immunity and virus persistence. *Future Virol* **13**, 493–503 (2018).
734 63. Yang, E. & Li, M. M. H. All About the RNA: Interferon-Stimulated Genes That Interfere With Viral
735 RNA Processes. *Front Immunol* **11**, 605024 (2020).
736 64. Abe, K. *et al.* Analysis of interferon-beta mRNA stability control after poly(I:C) stimulation using RNA
737 metabolic labeling by ethynyluridine. *Biochem Biophys Res Commun* **428**, 44–49 (2012).
738 65. Cabral-Piccin, M. P. *et al.* Primary role of type I interferons for the induction of functionally optimal
739 antigen-specific CD8+ T cells in HIV infection. *EBioMedicine* **91**, 104557 (2023).
740 66. Hemann, E. A. *et al.* A Small Molecule RIG-I Agonist Serves as an Adjuvant to Induce Broad
741 Multifaceted Influenza Virus Vaccine Immunity. *J Immunol* **210**, 1247–1256 (2023).

742 67. Proietti, E. *et al.* Type I IFN as a Natural Adjuvant for a Protective Immune Response: Lessons from
743 the Influenza Vaccine Model1. *The Journal of Immunology* **169**, 375–383 (2002).
744 68. Sasaki, E. *et al.* Systemically inoculated adjuvants stimulate pDC-dependent IgA response in local
745 site. *Mucosal Immunol* **16**, 275–286 (2023).
746
747

748 **Figure Legends**

749

750 **Figure 1: MK-8722 inhibits SARS-CoV-2 replication *in vitro.***

751 **A:** ***Schematic outline of the continuous treatment protocol with MK-8722***.

752 **B-D:** ***Dose dependent inhibition of Vero76 and Calu-3 cell infection with SARS-CoV2 by continuous***
753 ***treatment with MK-8722***. Inhibition of infection with indicated SARS-CoV-2 variant in Vero76 was
754 measured by flow cytometry (**B**) and that of Calu-3 by FISH-flow (**C-D**). n≥5 independent experiments.
755 Labelling for SARS-CoV-2 Spike (Black) and for viral RNA (Red).

756 **E:** ***Dose-dependent inhibition of viral genome release from Calu-3 cells*** infected with the Alpha variant
757 after continuous treatment with MK-8722 measured by quantification of *N* RNA in the supernatant by
758 RT-qPCR. n≥5 independent experiments.

759 **F-G:** ***Inhibition of viral replication after MK-8722 treatment.*** Cells were incubated with the indicated
760 SARS-CoV-2 variant in the absence or the presence of the drug (1 µM for Vero76 **(F)** and 5µM for Calu-3
761 cells **(G)**) for 1h at 4°C to synchronize infection and chased for 1h or for an additional 24h in the case of
762 Vero76 cells and for 32h in the case of Calu-3 cells at 37°C. *N* RNA was quantified in cellular extracts by
763 RT-qPCR. n≥5 independent experiments.

764 **H**: ***Schematic representation of the post-exposure treatment protocol with MK-8722.***

765 **I-J**: ***Post-exposure treatment with MK-8722 is sufficient to block infection by SARS-CoV-2.*** Cells were
766 left untreated or treated with MK-8722 (5 µM) either continuously with Alpha variant or treated post-
767 infection as in **G**. Infection was evaluated by quantification of Spike expression by flow cytometry (**I**) or
768 by RT-qPCR using the $2^{-\Delta\Delta Ct}$ method (**J**). Values represent infection inhibition. n≥6 independent
769 experiments. Shown are mean ± SEM.

770 ANOVA: * $p<0.05$, ** $p<0.01$, *** $p<0.001$, **** $p<0.0001$.

771

772 **Figure 2: MK-8722-dependent AMPK activation inhibits SARS-CoV-2 replication by inhibition of the**
773 **lipid biosynthetic pathway and restoration of the autophagy flux.**

774 **A**: **Activation or expression ratio of AMPK, ACC, raptor, ULK1, p62 and Nucleocapsid were analyzed by**
775 **western blot** in Vero76 and Calu-3 cells after continuous MK-8722 treatment as indicated in Figure 1A
776 Western blots were quantified by ImageJ, and each marker value in indicated condition was normalized
777 over corresponding marker expression value in the non-infected non-treated condition. Shown are
778 mean ± SEM. n≥2 independent experiments.

779 **B: *Quantification of the western blot presented as Heat maps:*** Heat maps represent the transformation
780 by Log2 of the expression/phosphorylation values quantified on each blot by ImageJ relative to
781 corresponding non-infected non-treated condition for Vero76 and Calu-3 cells. n≥2 independent
782 experiments. Student's *t*–test: * $p<0.05$, ** $p<0.01$.

783

784 **Figure 3: MK-8722 inhibition of SARS-CoV-2 is associated to decrease of lipid droplets and release of**
785 **defective viral particles.**
786 **A: *Morphological analyses.*** Calu-3 cells were infected with the SARS-CoV-2 Alpha variant in the
787 presence of a continuous treatment with MK-8722 (5 µM) or not. At 3dpi, lipids droplets, defined as
788 indicated in the method section, were stained with Nile Red lipophilic dye before cells fixation.
789 Nucleoprotein protein (Green) expression detected by immunofluorescence, Nile Red (Red) staining and
790 nuclei staining with DAPI (Blue) were observed by confocal microscopy. One representative field out of 5
791 observed per condition are presented. Bar: 20 µm. Shown are images representative of n=3
792 independent experiments.
793 **B: *Quantitative analysis of images*** shown in A using ImageJ of the number, area and intensity of lipid
794 droplets (LD), as defined in the method section within infected cells, characterized by the expression of
795 Nucleocapsid protein. Values were normalized to corresponding infected non-treated condition. n=3
796 independent experiments.
797 **C: *Lipid droplets and N-protein colocalization*.** The fraction of lipid droplets colocalizing in Nucleocapsid
798 staining and inversely were quantified using JACoP plugin from ImageJ software and corresponding
799 Manders' overlap coefficients (MOC) are presented.
800 **D**: ***Viral genomes released***. Cells were infected with the Alpha SARS-CoV-2 variant in the absence or in
801 the presence of a continuously treatment with MK-8722 at the indicated concentrations. Viral *N* RNA
802 released by Vero76 cells at 1dpi (upper panel) and Calu-3 cells at 4dpi (lower panel) cells were
803 quantified by RT-qPCR. n≥3 independent experiments.
804 **E: *Viral titres released*** by Vero76 (upper panel) and Calu-3 (lower panel) cells treated as above in (**D**).
805 n=3 independent experiments.
806 **F: *Infectious index of released viruses*** determined as described in the methods section using matched
807 viral titres and viral copy number values Vero76 (upper panel) and Calu-3 (lower panel) cells obtained as
808 in (**D**) and (**E**). n=4 independent experiments.
809

810 Student's *t*–test and Mann-Whitney * $p<0.05$, ** $p<0.01$, *** $p<0.001$, **** $p<0.0001$.

811

812

813 **Figure 4: MK-8722 treatment increases lysosomal degradation of viral components and restore type I**
814 **interferon response.**

815 **A: *Morphological analysis***: Calu-3 cells were infected with the SARS-CoV-2 Alpha variant in the presence
816 of a continuously treatment with MK-8722 (5 µM) or not. At 3dpi, cells were then fixed and LAMP1 (Red)
817 and Nucleocapside N (Green) protein expression was detected by immunofluorescence. Nuclei were
818 stained with DAPI (Blue). Cells were observed by confocal microscopy. One representative field out of 5
819 observed per condition is presented. Bar: 20 µm. Images representative of n=3 independent
820 experiments.

821 **B: *Quantitative analysis*** of images show in A using ImageJ of number, area and intensity of lysosomes,
822 identified as defined in the methods section, within infected cells, characterized by the expression of
823 Nucleocapsid protein. Values were normalized to infected non-treated condition. n=3 independent
824 experiments.

825 **C: *LAMP1 and N protein colocalization*.** The fraction lysosomal objects colocalizing with Nucleocapsid
826 staining and inversely were quantified using JACoP plugin from ImageJ software and corresponding
827 Manders' overlap coefficients (MOC) are presented. n=3 independent experiments.

828 **D: *Lysosomal activity.*** Calu-3 cells were infected with the indicated SARS-CoV-2 variant in the presence
829 of indicated MK-8722 concentration added at 24hpi and cultured for another 24h. Lysosomal activity
830 was then analysed using Lysotracker DND99 dye and quantified by flow cytometry. Shown are
831 lysotracker MFI collected from n≥5000 cells analysed. n=3 experiment.

832 **E: *IFN-I response***. Calu-3 cells were infected with SARS-CoV-2 Alpha variant in the presence of MK-8722
833 (5 µM) continuous treatment (dark orange) or initiated at 8hpi (light orange) or without treatment
834 (Blue). IFN-I response was evaluated by quantifying *IFNα*, *INFβ*, *Mx1* and *OAS1* mRNA by RT-qPCR of
835 indicated genes at 1dpi. Data represent the expression of each mRNA relative to *β-actin* mRNA levels,
836 and expressed following the $2^{-\Delta\Delta Ct}$ method. n=3 independent experiments.

837 ANOVA and Mann-Whitney * $p<0.05$, ** $p<0.01$, *** $p<0.001$, **** $p<0.0001$.

838

839 **Figure 5: MK-8722 treatment does not alter T cell response from vaccinated individuals against SARS-**
840 **CoV-2 *in vitro*.**

841 **A:** PBMCs from healthy SARS-CoV-2 vaccinated donors depleted in CD14 cells were stimulated for 6h
842 with anti-CD3 and anti-CD28 antibodies in the absence or in presence of MK-8722 (5 µM). IFNγ$^+$ and
843 CD107a$^+$ cell frequencies within CD4$^+$ and CD8$^+$ T cell populations were evaluated by flow cytometry. n=5
844 independent donors analysed in independent experiments.
845 **B:** CD14-depleted PBMCs from corresponding donors in **(A)** were stimulated for 6h with a T cell SARS-
846 CoV-2 spike peptide pool (Peptivator, Miltenyi), IFNγ$^+$ and CD107a$^+$ cell frequencies were quantified as in
847 (A). Activation levels are presented as activation index calculated as described in the methods section.
848 n≥3 independent donors analysed in independent experiments.
849 **C:** Caco2 cells were infected 2h with the Alpha variant of SARS-CoV-2 and treated post exposure (8hpi)
850 with MK-8722 (5 µM) alone or together with CD8$^+$ T cells from SARS-CoV-2 vaccinated individuals.
851 Infection was evaluated by quantification of Spike expression in cells at 2dpi by flow cytometry and
852 presented as inhibition of Spike expression frequency. n=5 independent donors performed in
853 independent experiments. Data presented are mean ± SEM.
854 ANOVA and *t*-test: * $p<0.05$, ** $p<0.01$, *** $p<0.001$, **** $p<0.0001$
855

856 **Supplementary Figure Legends**

857 ***Supplementary Figure S1: Kinetic of AMPK activation and downstream ACC phosphorylation*** evaluated
858 by western-blot after MK-8722 stimulation of Vero76.
859

860 ***Supplementary Figure S2: MK-8722 inhibits SARS-CoV-2 infection.***
861 **A:** Gating strategies used to analyse infection inhibition by MK-7822 treatment in Vero76 cells in Figure
862 1B.
863 **B:** Cells were treated as indicated in Figure 1B. Frequencies of infection in corresponding experimental
864 sample shown in Figure 1B were measured by SARS-CoV-2 Spike detection in Vero76 cells. Shown are
865 mean ± SEM. n=4 independent experiments.
866 **C:** Gating strategies used to analyse infection inhibition by MK-7822 treatment in Calu-3 cells in Figure
867 1C.
868 **D-E:** Cells were treated as indicated in Figure 1B and C. Frequencies of infection in corresponding
869 experimental sample shown in Figure 1B and C were measured by dual detection of Spike (Black) and
870 viral RNA (Red) using Fish-flow in Calu-3 cells infected by Alpha **(D)** or Omicron **(E)** variant, quantified by
871 flow cytometry. Shown are mean ± SEM. n=4 independent experiments.

872 **F**: Inhibition of infection by Remdesevir. Calu-3 cells were treated with Remdesivir (0.1 µM or 1 µM) 1h
873 prior and during the 2h of inoculation with SARS-CoV-2 Alpha variant. After virus removal, treatment
874 with Remdesivir at indicated concentration was continued. At 4dpi, infection was quantified by dual
875 detection of Spike (Black) and viral RNA (Red) in Fish-flow quantified by flow cytometry. Shown are
876 mean ± SEM of Spike and vRNA frequency (left) and infection inhibition (right). n=3 independent
877 experiments.
878 **H-I:** ACE2 expression and viability were evaluated in Vero76 cells after 24h or in Calu-3 cells after 4days
879 of MK-8722 continuous treatment (1 µM or 5 µM respectively) by flow cytometry. ACE2 expression is
880 expressed as MFI (**F**) and viability as frequency of cells non-stained by the amine-reactive dye Viobility
881 (**G**). n=3 independent experiments.
882
883 Shown are mean ± SEM. ANOVA: * $p<0.05$, ** $p<0.01$, *** $p<0.001$, **** $p<0.0001$.

884 **Supplementary Figure S3:** ***Evaluation of MK-8722 activity on cellular pathways downstream AMPK***
885 ***activation by western blot*** of ACC, ULK1, Raptor and AMPK phosphorylation, and Nucleocapsid protein
886 N and autophagy cargo receptor p62 expression in Vero76 **(A)** and Calu-3 cells **(B)** infected or not and
887 continuously treated or not with MK-8722 (5 µM) as indicated. The image shown is a montage of non-
888 adjacent from same western blots experiments used to evaluate each protein and, when indicated,
889 corresponding phosphorylated form.

890 ***Supplementary Figure S4: MK-8722 treatment decreases lipid droplet distribution in uninfected Calu-3***
891 ***cells.***
892 **A:** Cells were left uninfected and treated with MK-8722 (5 µM) or not and analyzed as indicated in Figure
893 3. Representative fields for Nile Red (Red) and Nucleocapsid N protein immunodetection (Green) imaged
894 by confocal microscopy are shown. Nuclei were stained with DAPI (Blue). Bars: 20 µm
895 **B:** Cells were treated and labelled as described in Figure 3. Total intensity of total Nile Red staining per
896 cell was calculated in ImageJ for non-infected non-treated (Ni-NT), infected non-treated (Infected-NT)
897 and Infected MK-8722 treated conditions. Values were normalized to the mean of non-infected non-
898 treated condition (Ni-NT). Shown are mean ± SEM. n= 3 independent experiments. ANOVA: $p<0.05$.
899
900 ***Supplementary Figure S5: MK-8722 impacts lysosomal parameters in Calu-3 cells.***

901 **A:** Cells were left uninfected but treated with MK-8722 (5 µM) or not and analysed as indicated in Figure
902 4. Representative fields for LAMP1 (Red) and Nucleocapsid N protein (Green) immunodetection imaged
903 by confocal microscopy are shown. Nuclei were stained with DAPI (Blue). Bars: 20 µm
904 **B:** Cells were treated and labelled as described in Figure 4. Total intensity of total LAMP1 staining per
905 cell was calculated in ImageJ for non-infected non-treated condition (Ni-NT), infected non-treated
906 (Infected-NT) and treated with 5 µM MK-8722 (Infected-MK-8722). Values were normalized to
907 corresponding non-infected non-treated condition. n≥3 independent experiments. Shown are mean ±
908 SEM. ANOVA: ** $p<0.01$ and *** $p<0.001$.
909
910 ***Supplementary Figure S6: Evaluation of nucleocapsid-specific T cell response in SARS-CoV-2 vaccinated***
911 ***individuals upon MK-8722 treatment ex vivo.***
912 **A:** PBMCs from healthy donors were cultivated for 6h indicated concentration of MK-8722 or
913 corresponding DMSO serving as carrier. CD4 and CD8 T cells activation (CD107a and IFNg expression)
914 was monitored by flow cytometry.
915 **B:** Gating strategy to investigate $CD4^+$ and $CD8^+$ T cell responses stimulation after activation with anti-
916 CD3/anti-CD28 antibodies (Transact) with or without MK-8722 treatment as analysed in Figure 5A.
917 **C:** CD14-depleted PBMCs corresponding to donors used in Figure 5 were stimulated as described in
918 Figure 5B but with T cell Nucleocapsid peptides (Peptivator, Miltenyi), and monitored by flow cytometry
919 for IFNγ and CD107a expression. Activation levels are presented as activation index as described in the
920 methods section. n≥3 independent donors.
921
922 ***Supplementary Figure S7: Gating strategy for combined MK-8722 treatment and $CD8^+$ T cell antiviral***
923 ***activity in coculture.***
924 Gating strategy to quantify the inhibition of Caco2 cells infection in the presence of MK-8722 and/or
925 $CD8^+$ T cells from vaccinated individuals shown in Figure 5C. Infection was evaluated within Caco2 cells
926 corresponding to the $CD3^-CD8^-$ population. The low number of $CD8^+$ T cells (around 150) prevented us
927 from investigating their activation level.

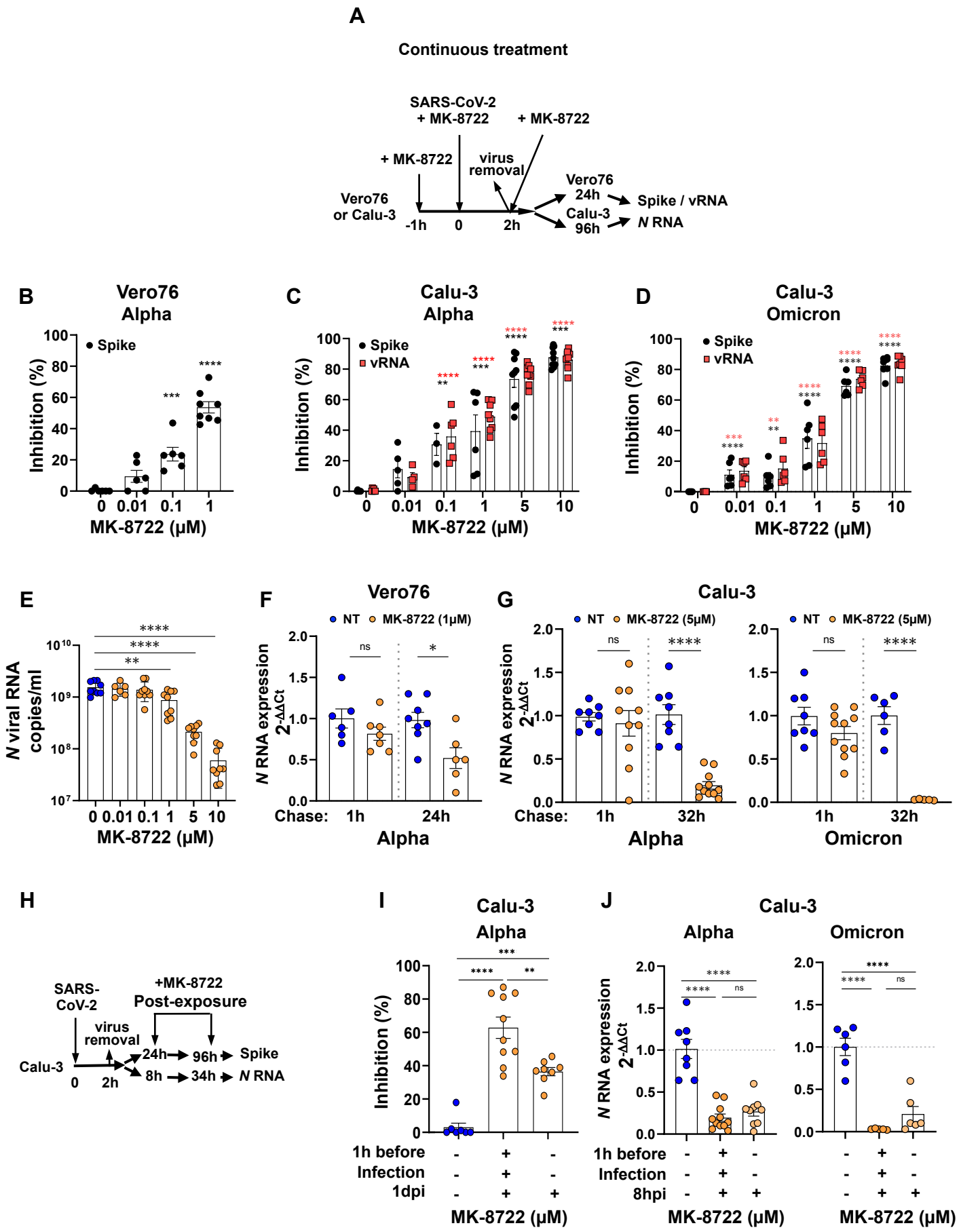
A
Continuous treatment
SARS-CoV-2
+ MK-8722
+ MK-8722
+ MK-8722
virus
removal
Vero76
or Calu-3
-1h
0
2h
Vero76
24h
Spike / vRNA
Calu-3
96h
N RNA
B
Vero76
Alpha
Spike
Inhibition (%)
MK-8722 (μM)
C
Calu-3
Alpha
Spike
vRNA
Inhibition (%)
MK-8722 (μM)
D
Calu-3
Omicron
Spike
vRNA
Inhibition (%)
MK-8722 (μM)
E
N viral RNA
copies/ml
MK-8722 (μM)
F
Vero76
NT
MK-8722 (1μM)
N RNA expression
2-ΔΔCt
Chase:
1h
24h
Alpha
G
Calu-3
NT
MK-8722 (5μM)
N RNA expression
2-ΔΔCt
Chase:
1h
32h
Alpha
Omicron
H
SARS-
CoV-2
+MK-8722
Post-exposure
virus
removal
Calu-3
0
2h
24h
96h
Spike
8h
34h
N RNA
I
Calu-3
Alpha
Inhibition (%)
1h before
Infection
1dpi
MK-8722 (μM)
J
Calu-3
Alpha
Omicron
N RNA expression
2-ΔΔCt
1h before
Infection
8hpi
MK-8722 (μM)
MK-8722 (μM)

Figure 1

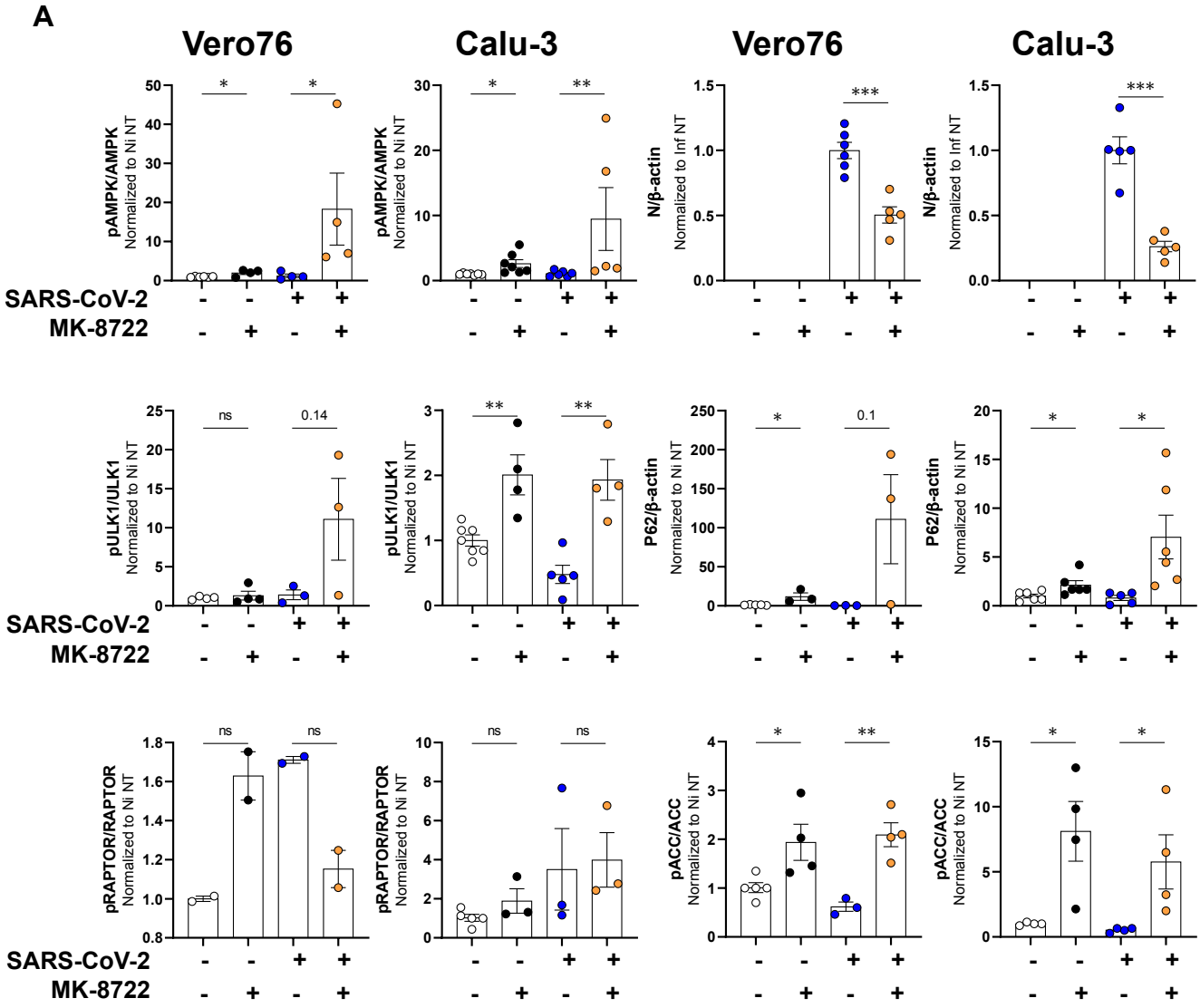
A
Vero76
Calu-3
Vero76
Calu-3
pAMPK/AMPK
Normalized to Ni NT
N/β-actin
Normalized to Inf NT
pULK1/ULK1
P62/β-actin
pRAPTOR/RAPTOR
pACC/ACC
SARS-CoV-2
MK-8722
ns
0.14
0.1

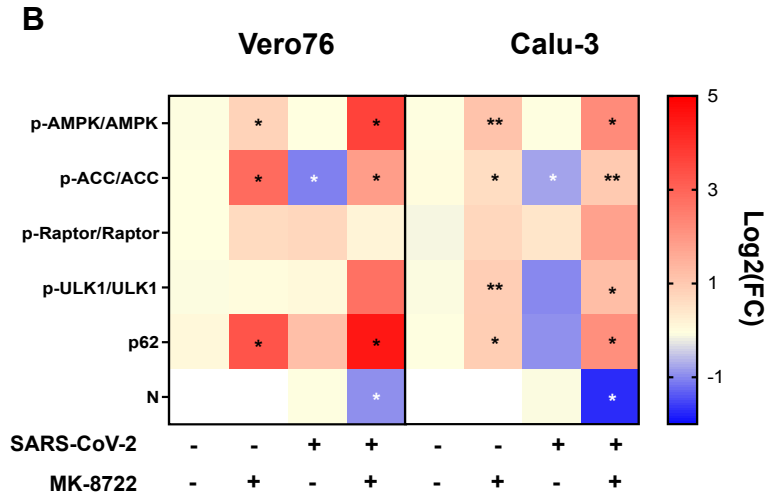
B
Vero76
Calu-3
p-AMPK/AMPK
p-ACC/ACC
p-Raptor/Raptor
p-ULK1/ULK1
p62
N
SARS-CoV-2
MK-8722
Log2(FC)

Figure 2

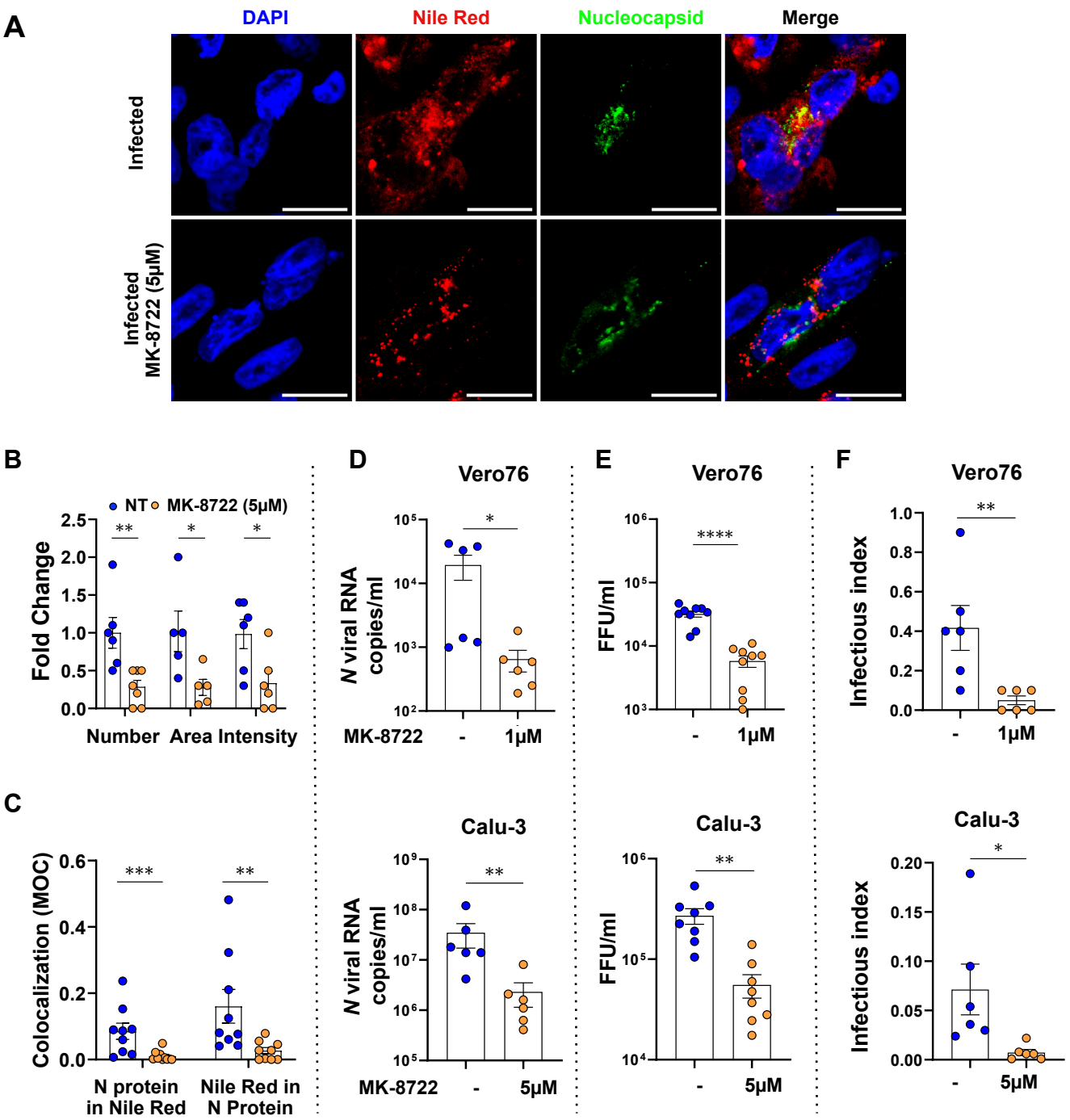
A
DAPI
Nile Red
Nucleocapsid
Merge
Infected
Infected MK-8722 (5μM)
B
NT
MK-8722 (5μM)
Fold Change
Number
Area
Intensity
C
Colocalization (MOC)
N protein in Nile Red
Nile Red in N Protein
D
Vero76
Calu-3
N viral RNA copies/ml
MK-8722
-
1μM
5μM
E
FFU/ml
F
Infectious index

Figure 3

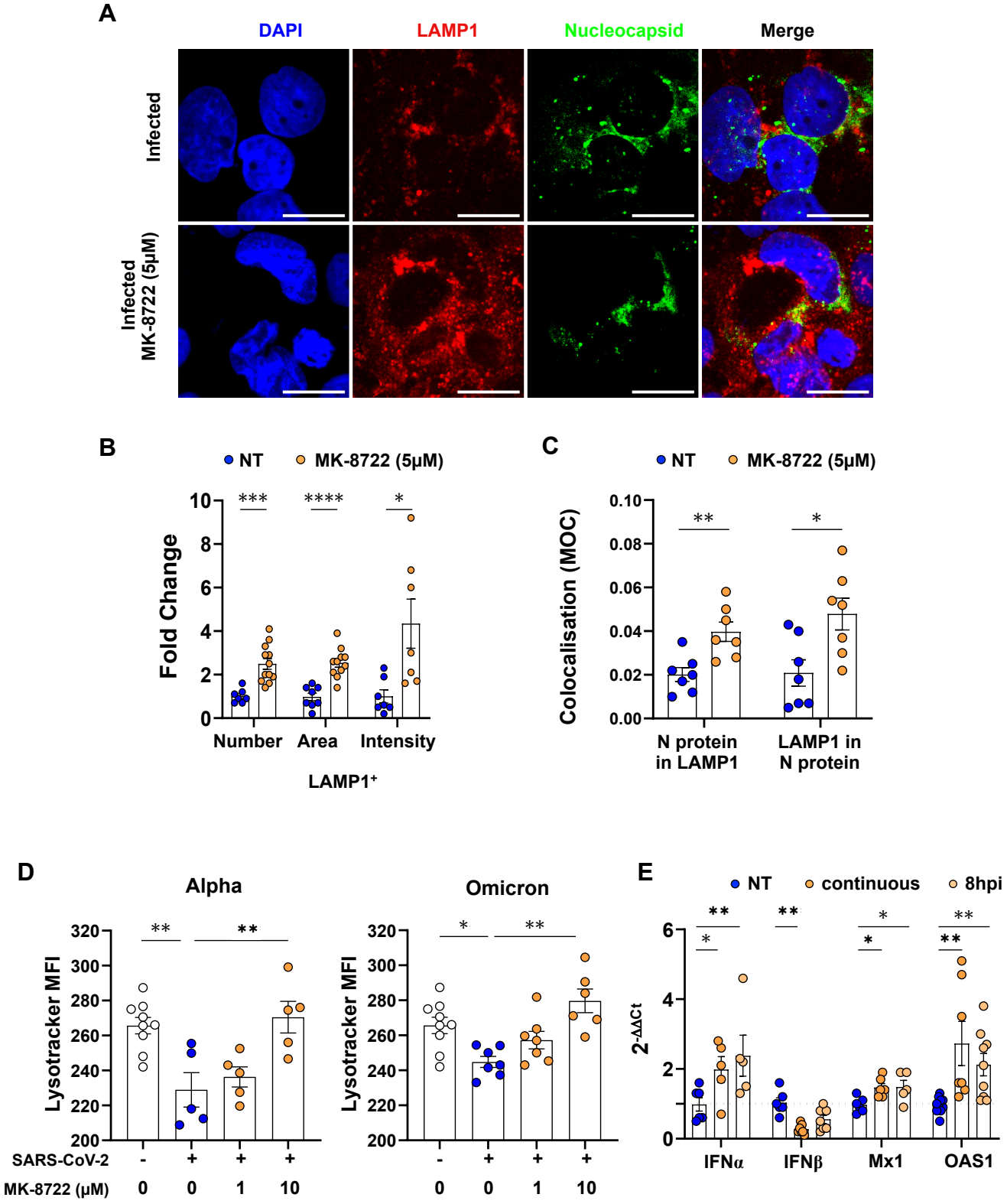
A
DAPI
LAMP1
Nucleocapsid
Merge
Infected
Infected
MK-8722 (5μM)
B
NT
MK-8722 (5μM)
Fold Change
Number
Area
Intensity
LAMP1+
C
NT
MK-8722 (5μM)
Colocalisation (MOC)
N protein in LAMP1
LAMP1 in N protein
D
Alpha
Omicron
Lysotracker MFI
SARS-CoV-2
MK-8722 (μM)
E
NT
continuous
8hpi
2-ΔΔCt
IFNα
IFNβ
Mx1
OAS1

Figure 4

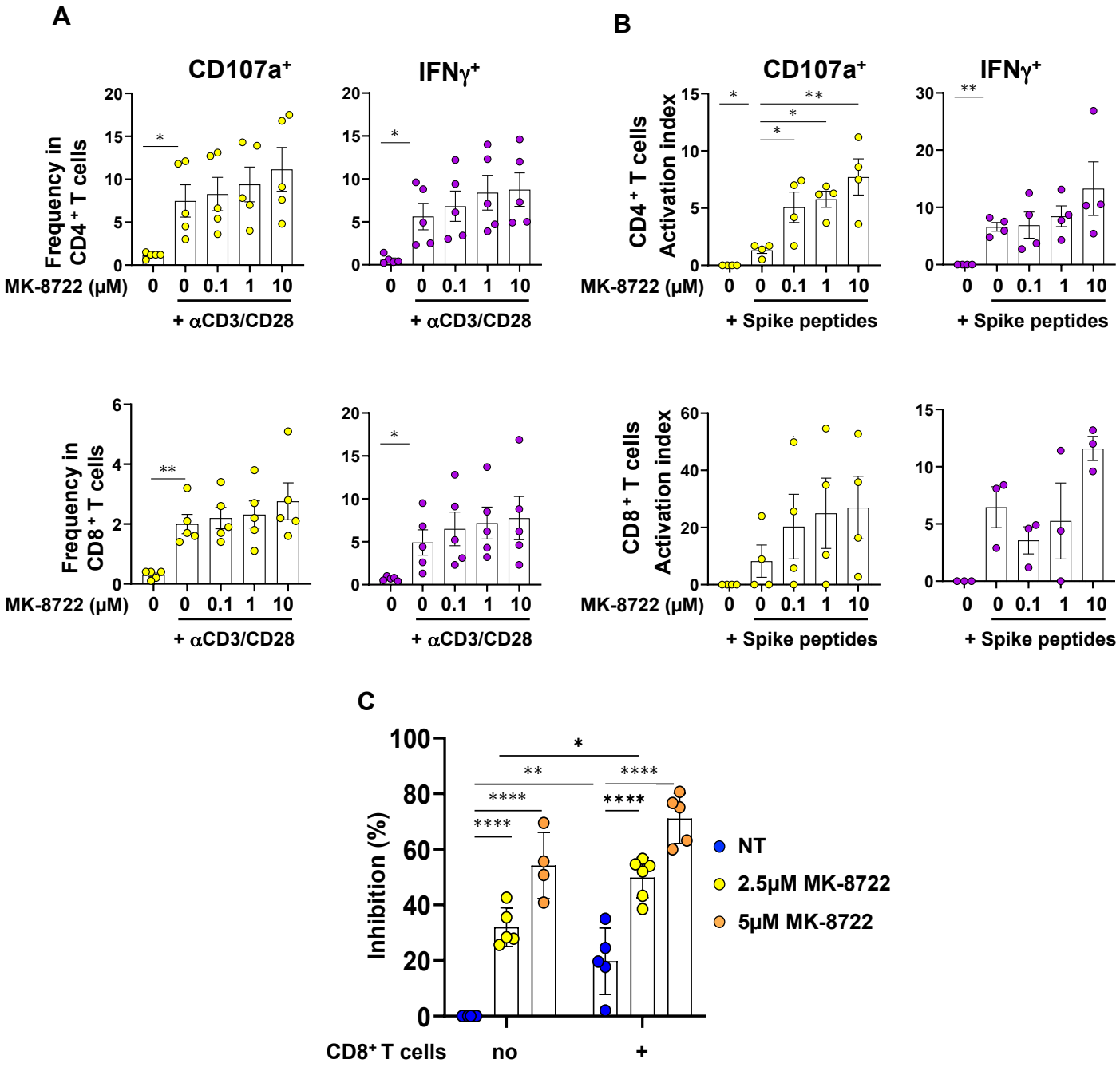
A
CD107a+
IFNγ+
Frequency in CD4+ T cells
MK-8722 (μM)
0 0 0.1 1 10
+ αCD3/CD28
B
CD4+ T cells Activation index
+ Spike peptides
Frequency in CD8+ T cells
CD8+ T cells Activation index
C
Inhibition (%)
NT
2.5μM MK-8722
5μM MK-8722
CD8+ T cells
no
+

Figure 5

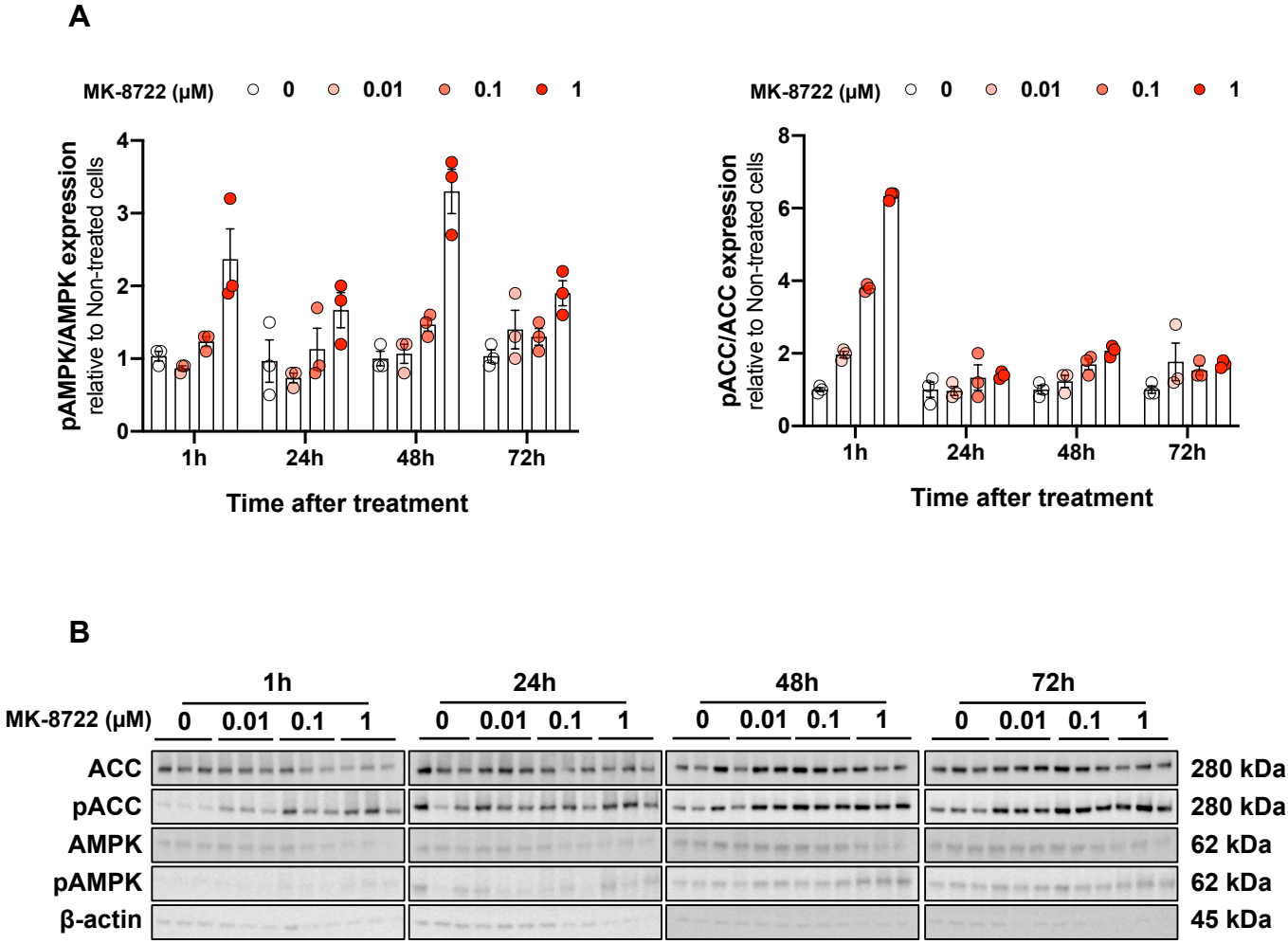
A
MK-8722 (μM)
0
0.01
0.1
1
pAMPK/AMPK expression
relative to Non-treated cells
1h
24h
48h
72h
Time after treatment
pACC/ACC expression
relative to Non-treated cells
B
ACC
pACC
AMPK
pAMPK
β-actin
280 kDa
280 kDa
62 kDa
62 kDa
45 kDa

Figure S1

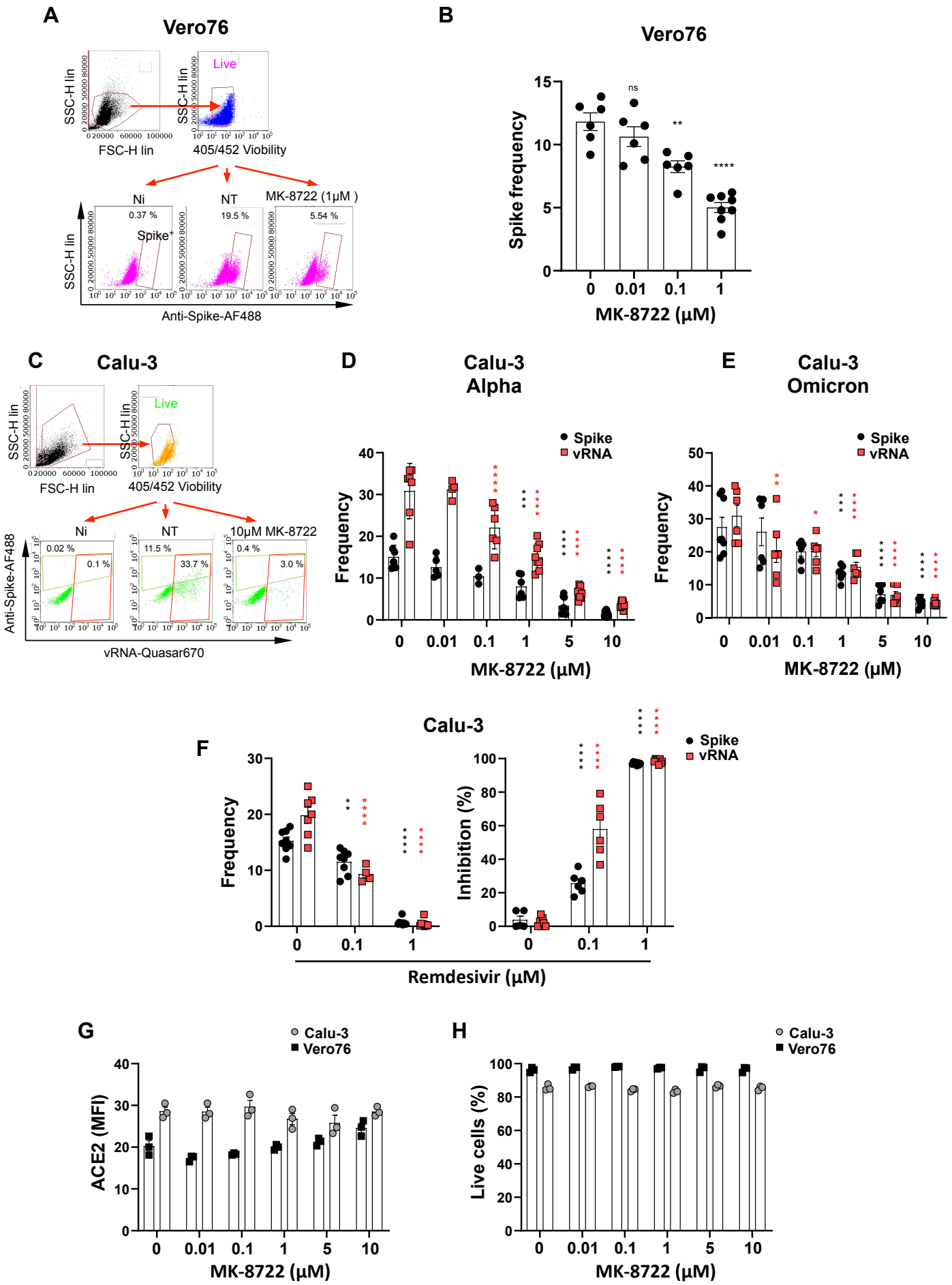
A
Vero76
SSC-H lin
FSC-H lin
Live
405/452 Viobility
Ni
NT
MK-8722 (1μM)
0.37 %
19.5 %
5.54 %
Spike+
Anti-Spike-AF488
B
Vero76
Spike frequency
ns
**
****
MK-8722 (μM)
C
Calu-3
10μM MK-8722
0.02 %
0.1 %
11.5 %
33.7 %
0.4 %
3.0 %
vRNA-Quasar670
D
Calu-3
Alpha
Spike
vRNA
Frequency
MK-8722 (μM)
E
Calu-3
Omicron
F
Calu-3
Inhibition (%)
Remdesivir (μM)
G
Calu-3
Vero76
ACE2 (MFI)
H
Live cells (%)

Figure S2

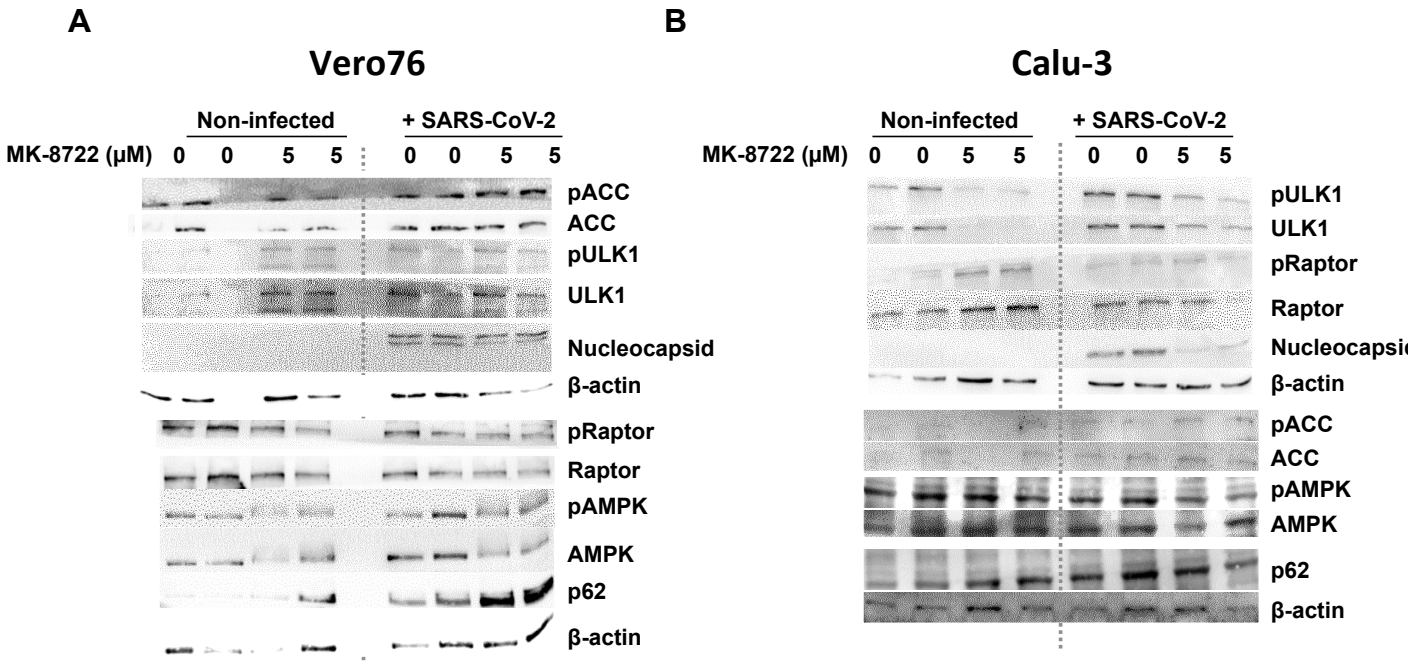
A
Vero76
Non-infected
+ SARS-CoV-2
MK-8722 (μM) 0 0 5 5 0 0 5 5
pACC
ACC
pULK1
ULK1
Nucleocapsid
β-actin
pRaptor
Raptor
pAMPK
AMPK
p62
β-actin
B
Calu-3
Non-infected
+ SARS-CoV-2
MK-8722 (μM) 0 0 5 5 0 0 5 5
pULK1
ULK1
pRaptor
Raptor
Nucleocapsid
β-actin
pACC
ACC
pAMPK
AMPK
p62
β-actin

Figure S3

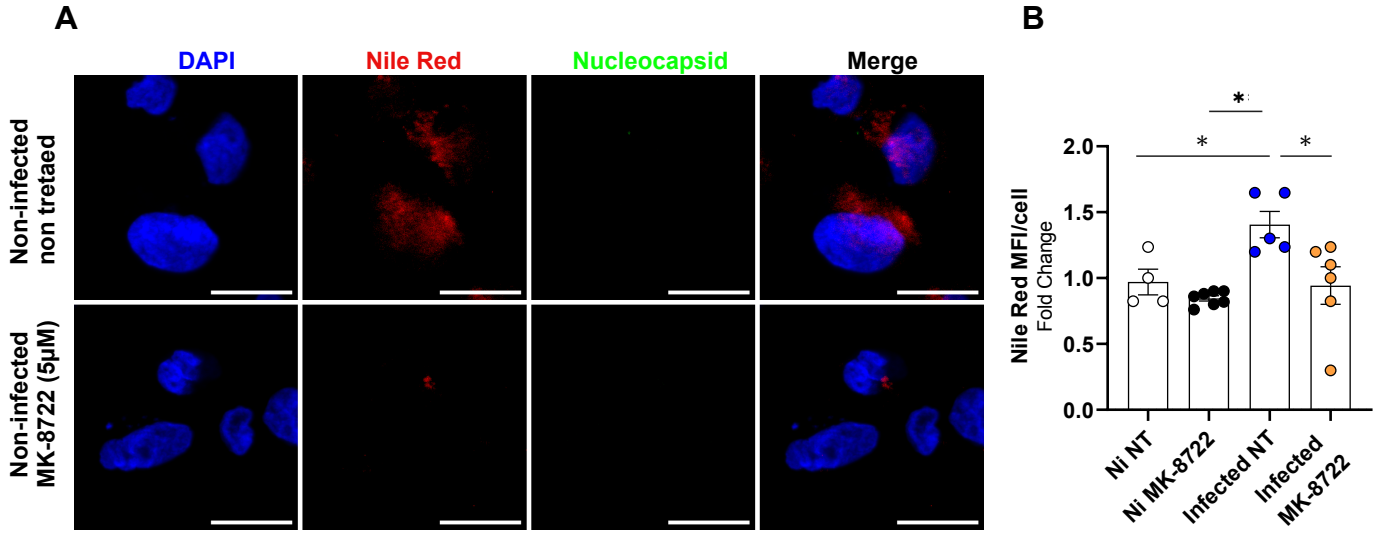
A
DAPI
Nile Red
Nucleocapsid
Merge
Non-infected non tretaed
Non-infected MK-8722 (5μM)
B
Nile Red MFI/cell
Fold Change
2.0
1.5
1.0
0.5
0.0
*
*
*
Ni NT
Ni MK-8722
Infected NT
Infected MK-8722

Figure S4

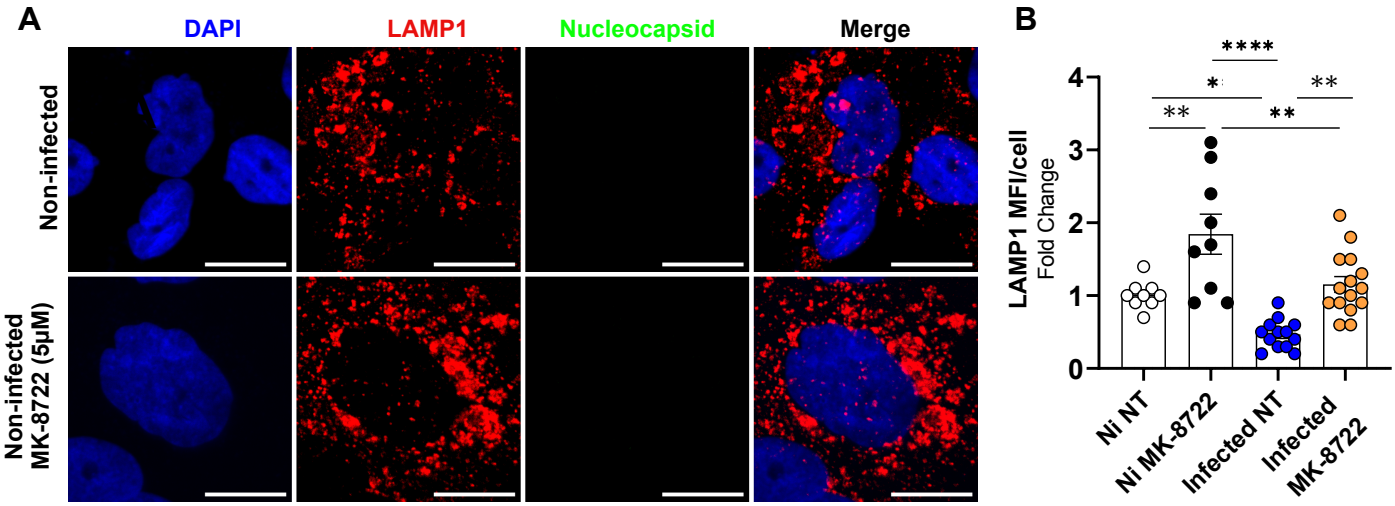
A
DAPI
LAMP1
Nucleocapsid
Merge
Non-infected
Non-infected
MK-8722 (5μM)
B
LAMP1 MFI/cell
Fold Change
0
1
2
3
4
****
*
**
**
**
Ni NT
Ni MK-8722
Infected NT
Infected
MK-8722

Figure S5

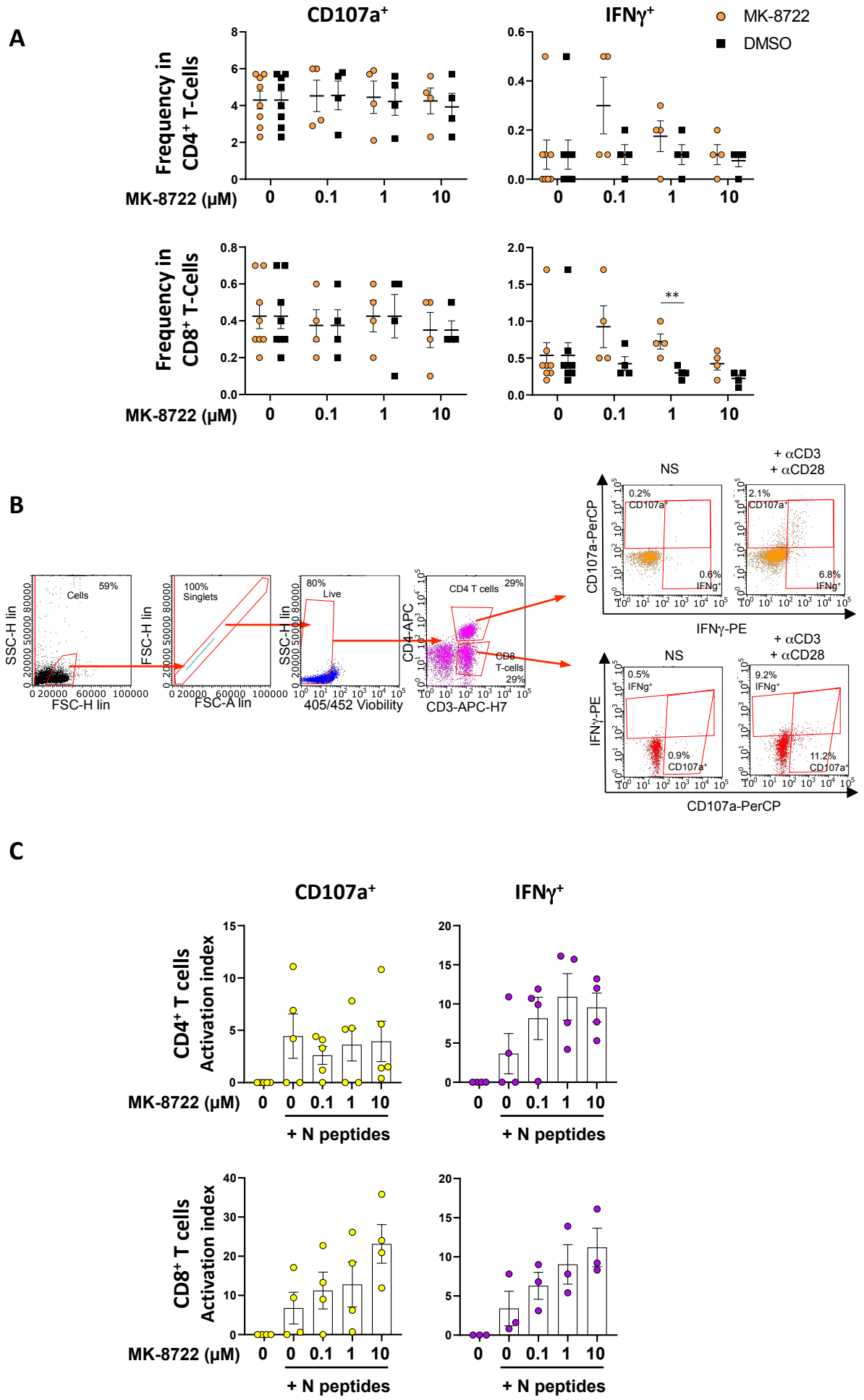
A
CD107a+
IFNγ+
MK-8722
DMSO
Frequency in CD4+ T-Cells
Frequency in CD8+ T-Cells
MK-8722 (μM)
0
0.1
1
10
**
B
SSC-H lin
FSC-H lin
Cells
59%
100% Singlets
FSC-A lin
80% Live
405/452 Viability
CD4-APC
CD3-APC-H7
CD4 T cells
29%
CD8 T-cells
29%
NS
+ αCD3 + αCD28
CD107a-PerCP
IFNγ-PE
0.2% CD107a+
0.6% IFNg+
2.1% CD107a+
6.8% IFNg+
0.5% IFNg+
0.9% CD107a+
9.2% IFNg+
11.2% CD107a+
C
CD107a+
IFNγ+
CD4+ T cells Activation index
CD8+ T cells Activation index
MK-8722 (μM)
+ N peptides

Figure S6

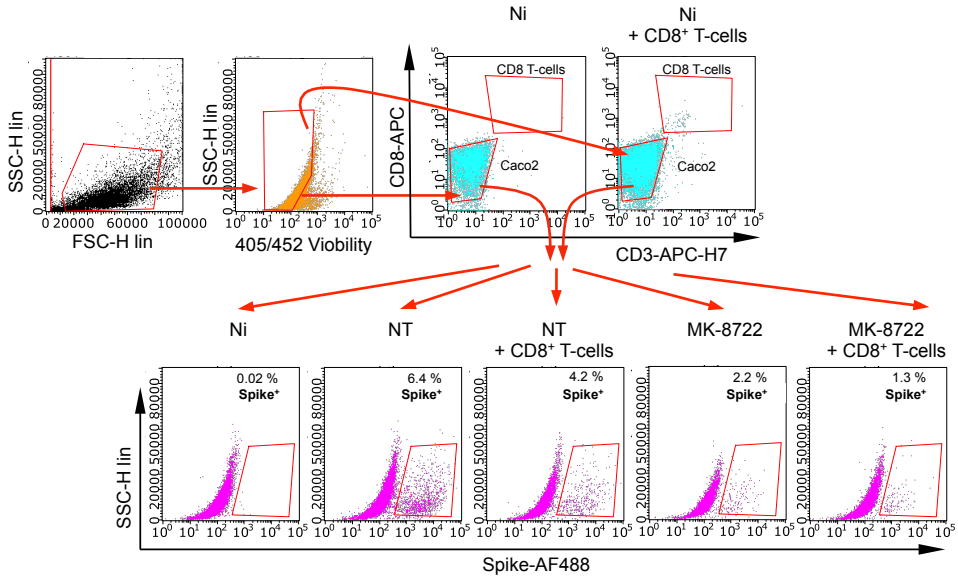
Ni
Ni
+ CD8+ T-cells
SSC-H lin
FSC-H lin
405/452 Viobility
CD8-APC
CD8 T-cells
Caco2
CD3-APC-H7
Ni
NT
NT
+ CD8+ T-cells
MK-8722
MK-8722
+ CD8+ T-cells
0.02 %
Spike+
6.4 %
Spike+
4.2 %
Spike+
2.2 %
Spike+
1.3 %
Spike+
Spike-AF488

Figure S7